

Removing nodal and support-mismatch pathologies in Variational Monte Carlo via blurred sampling

Zhou-Quan Wan^{Ⓧ,*}, Roeland Wiersema^{Ⓧ,†} and Shiwei Zhang^{Ⓧ,‡}

Center for Computational Quantum Physics, Flatiron Institute, New York, NY 10010, USA

(Dated: March 20, 2026)

Variational Monte Carlo (VMC) is a powerful and fast-growing method for optimizing and evolving parameterized many-body wave functions, especially with modern neural-network quantum states. In practice, however, the stochastic estimators that form the backbone of the method can become unstable or biased due to the presence of nodes, a ubiquitous feature of quantum wave functions. In the continuum, this results in heavy-tailed estimators with potentially divergent variances, while in discrete Hilbert spaces the sampling distribution can miss parts of the support needed to form unbiased estimators. These statistical pathologies lead to unreliable optimization trajectories in stochastic reconfiguration or incorrect variational dynamics in time-dependent Variational Monte Carlo (t-VMC), and severely limit the power of the numerical simulations. We introduce blurred sampling to address these difficulties. The method has a number of rigorous properties that make it well-behaved, effective and efficient. Additionally it is a post-processing approach that can be used without modifying the underlying sampler and incurs only minimal overhead. We demonstrate its effectiveness on several representative examples where standard sampling approaches are known to fail, and apply it to large-scale problems in spin dynamics. This work establishes a broadly applicable framework for robust VMC and t-VMC calculations.

I. INTRODUCTION

Variational Monte Carlo (VMC) provides a powerful framework for studying interacting quantum many-body systems by combining variational parameterizations of the wave function with stochastic sampling, thereby circumventing the exponential growth of Hilbert space [1, 2]. Recent advances in highly expressive variational ansätze—most notably neural-network quantum states—together with rapid progress in machine learning techniques and computational infrastructure, have substantially expanded the scope of VMC [3]. Within a unified Monte Carlo framework, VMC now enables accurate calculations of ground and excited states, real- and imaginary-time dynamics, and finite-temperature properties [3–17]. As a result, VMC has found broad applications across condensed matter physics [18–29], quantum chemistry [30–36], cold-atom or electron gas systems [37–47] and quantum simulation [48–50].

Despite this versatility, the reliability of VMC ultimately hinges on the statistical properties of its Monte Carlo estimators. Central quantities entering stochastic reconfiguration and time-dependent variational dynamics—such as energy gradients and variational forces—are expressed as ratios of wave-function amplitudes [3, 9, 13, 51]. Whenever the wave function develops nodes, these ratios become singular. Such nodal structures are ubiquitous in fermionic systems, frustrated magnets, and systems with sign structure enforced by symmetry or gauge fields. Near nodes, statistical fluctuations can be-

come heavy-tailed and may even acquire infinite variance in continuum settings [52–55]. In discrete configuration spaces, a related but more severe pathology can arise: if the support of the wave function does not coincide with that of the Hamiltonian action, the resulting estimators remain biased even in the infinite-sample limit [56, 57]. These statistical pathologies directly destabilize gradient-based optimization and variational time evolution, limiting the robustness and reliability of VMC.

Considerable effort has therefore been devoted to mitigating these instabilities. Some approaches modify the estimator directly through explicit regularization [58] or variance-reduction techniques such as control variates [56, 59]. More commonly, the problem is addressed through importance-sampling strategies that replace the original sampling distribution by a modified reference measure [60–65]. While these approaches can alleviate specific pathologies, they introduce competing requirements which are difficult to satisfy simultaneously. In practice, residual bias or variance amplification persists, and significant modification to the algorithm and additional computational overhead are often incurred. A broadly applicable and structurally robust solution to nodal instabilities in VMC remains lacking, which hinders progress in many application areas.

In this work, we introduce *blurred sampling* to address this challenge. Figure 1 provides a schematic illustration of the new approach. Rather than adding explicit regularization to the estimator or globally redefining the sampling distribution, blurred sampling applies a single local mixing step to Monte Carlo configurations as a post-processing operation. This procedure induces an implicit reference measure that regularizes nodal singularities at their origin while leaving the underlying sampling dynamics unchanged. We show that the resulting reweighting factors are strictly bounded, which ensures a finite ef-

* zwan@flatironinstitute.org

† rwiersema@flatironinstitute.org; Z.-Q.W. and R.W. contributed equally to this work.

‡ szhang@flatironinstitute.org

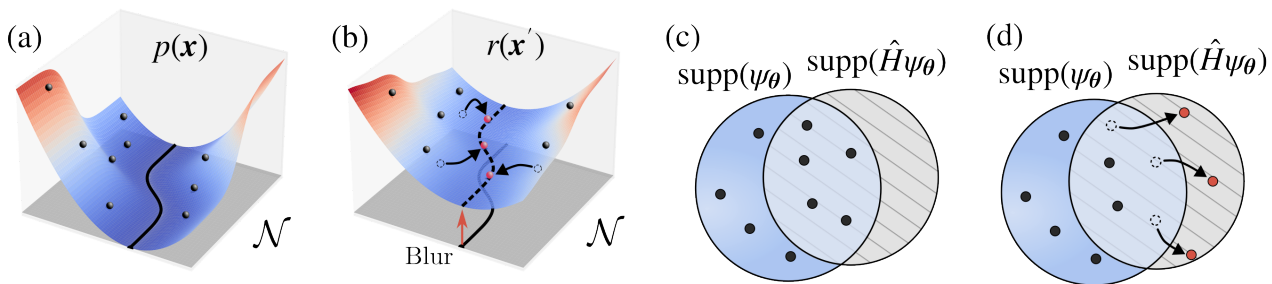


FIG. 1. Statistical pathologies and their resolution via blurred sampling. (a) Nodal hypersurfaces lead to divergences in ratio-type estimators due to vanishing probability density $p(\mathbf{x})$. (b) Blurred sampling locally perturbs the configurations, assigning finite probability to the original nodal set, regularizing the divergence. (c) The supports of ψ_θ and $\hat{H}\psi_\theta$ may not coincide (shaded region), resulting in a bias due to support mismatch, see Eq. (4). (d) Blurred sampling exploits the connectivity of \hat{H} , allowing configurations in $\text{supp}(\psi_\theta)$ to access the mismatched region of $\text{supp}(\hat{H}\psi_\theta)$, eliminating the bias.

fective sample size and resolves both infinite-variance behavior and support-mismatch bias. Because the method is implemented as a post-processing step, it preserves the computational scaling of standard VMC and, in discrete configuration spaces, can often be realized without additional wave-function evaluations. This design allows blurred sampling to integrate seamlessly with existing variational ansätze, optimization schemes, real- and imaginary-time dynamics, and modern sampling architectures [66, 67], including autoregressive models [68–74].

As we demonstrate below through theoretical analysis and numerical examples, blurred sampling restores stable and accurate simulations in regimes where conventional VMC breaks down. It provides a broadly applicable and scalable framework for achieving reliable simulations in variational Monte Carlo and neural quantum states, which will enable a wide range of applications across disciplines in quantum science.

II. BACKGROUND AND PRELIMINARIES

A. Variational Monte Carlo

In the general VMC framework, the many-body state is approximated by a parameterized wave function $|\psi_\theta\rangle = \sum_{\mathbf{x}} \psi_\theta(\mathbf{x}) |\mathbf{x}\rangle$ in the computational basis $\{|\mathbf{x}\rangle\}$, where the variational parameters $\theta \in \mathbb{C}^{N_{\text{para}}}$ are taken to be complex-valued, with real parameterizations recovered as a special case, and the sum over \mathbf{x} can be either discrete or continuous (integral). The optimization of the variational energy $E_\theta \equiv \frac{\langle \psi_\theta | \hat{H} | \psi_\theta \rangle}{\langle \psi_\theta | \psi_\theta \rangle}$ and the real- or imaginary-time dynamics are governed by two fundamental objects: the variational force $\mathbf{F} \equiv \partial_{\theta^*} E_\theta$ and the quantum geometric tensor (QGT) \mathbf{S} . They are defined as

$$\begin{aligned} F_i &= \frac{\langle \partial_{\theta_i} \psi_\theta | \hat{H} | \psi_\theta \rangle}{\langle \psi_\theta | \psi_\theta \rangle} - \frac{\langle \partial_{\theta_i} \psi_\theta | \psi_\theta \rangle \langle \psi_\theta | \hat{H} | \psi_\theta \rangle}{\langle \psi_\theta | \psi_\theta \rangle^2}, \\ S_{ij} &= \frac{\langle \partial_{\theta_i} \psi_\theta | \partial_{\theta_j} \psi_\theta \rangle}{\langle \psi_\theta | \psi_\theta \rangle} - \frac{\langle \partial_{\theta_i} \psi_\theta | \psi_\theta \rangle \langle \psi_\theta | \partial_{\theta_j} \psi_\theta \rangle}{\langle \psi_\theta | \psi_\theta \rangle^2}. \end{aligned} \quad (1)$$

These quantities determine the dynamics of parameters in stochastic reconfiguration (SR) and time-dependent VMC (t-VMC) through

$$S_{ij} \dot{\theta}_j = -\xi F_i, \quad (2)$$

which is called the time-dependent variational principle (TDVP) equation [3, 9, 12, 13, 75]. The choice $\xi = 1$ corresponds to the imaginary-time evolution (i.e., SR), and $\xi = i$ yields real-time dynamics.

In VMC, these quantities are evaluated by Monte Carlo sampling from the Born distribution $p(\mathbf{x}) = |\psi_\theta(\mathbf{x})|^2 / \sum_{\mathbf{x}} |\psi_\theta(\mathbf{x})|^2$. The estimators take the covariance form

$$\begin{aligned} F_i^{\text{MC}} &= \langle \mathcal{O}_i^*(\mathbf{x}) E_{\text{loc}}(\mathbf{x}) \rangle_p - \langle \mathcal{O}_i^*(\mathbf{x}) \rangle_p \langle E_{\text{loc}}(\mathbf{x}) \rangle_p, \\ S_{ij}^{\text{MC}} &= \langle \mathcal{O}_i^*(\mathbf{x}) \mathcal{O}_j(\mathbf{x}) \rangle_p - \langle \mathcal{O}_i^*(\mathbf{x}) \rangle_p \langle \mathcal{O}_j(\mathbf{x}) \rangle_p, \end{aligned} \quad (3)$$

where $\langle \cdot \rangle_p$ denotes expectation with respect to $p(\mathbf{x})$, $\mathcal{O}_i(\mathbf{x}) \equiv \partial_{\theta_i} \psi_\theta(\mathbf{x}) / \psi_\theta(\mathbf{x})$ is the logarithmic derivative, and $E_{\text{loc}}(\mathbf{x}) \equiv \langle \mathbf{x} | \hat{H} | \psi_\theta \rangle / \psi_\theta(\mathbf{x})$ is the local energy.

This representation makes the origin of statistical pathologies transparent: both E_{loc} and \mathcal{O}_i contain divisions by $\psi_\theta(\mathbf{x})$, so the corresponding ratio-type estimators can diverge in the vicinity of wave-function nodes, i.e., when $|\psi_\theta(\mathbf{x})| \rightarrow 0$. As a consequence, the stochastic estimators entering VMC can often become ill-behaved, as we discuss further in the next section.

B. Statistical Pathologies

These pathologies take different forms depending on the structure of the configuration space. We distinguish between continuum and discrete settings in turn.

Infinite variance in continuum systems. In continuum fermionic systems, the wave function $\psi_\theta(\mathbf{x})$ depends continuously on the particle coordinates. Fermionic statistics enforces the presence of nodal sets $\mathcal{N} \equiv \{\mathbf{x} | \psi_\theta(\mathbf{x}) = 0\}$ (see Fig. 1(a)), whose geometry has been extensively studied [76–79]. In the vicinity of a node,

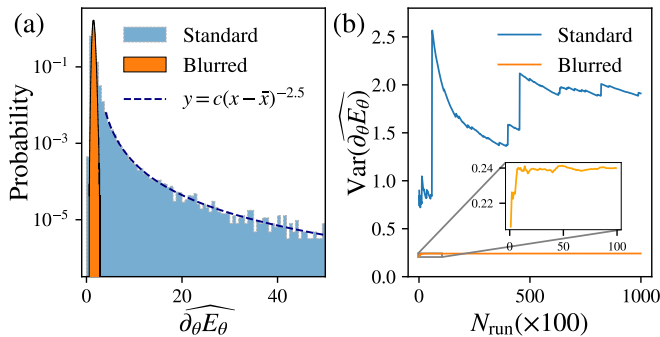


FIG. 2. Pedagogical example in the continuum. We consider two non-interacting spinless fermions on a ring, with the Hamiltonian $\hat{H} = -\frac{1}{2}(\partial_1^2 + \partial_2^2)$, and variational ansatz $\psi_\theta(x_1, x_2) = \cos(\theta) \sin(x_1 - x_2) + \sin(\theta) \sin(2x_1 - 2x_2)$, $x_{1,2} \in [0, 2\pi]$. (a) Distribution of the gradient estimator based on 1000 samples at $\theta = \pi/4$. Standard sampling exhibits a heavy-tailed distribution with exponent $\alpha = 1.5$, while blurred sampling yields a finite-variance estimator. (b) Estimated variance versus number of runs; Standard sampling does not converge.

the wave function vanishes linearly in the normal direction, $|\psi_\theta| \propto d$, where d denotes the distance to the nodal set. Consequently, ratio-type quantities in Eq. (3) diverge as $|E_{\text{loc}}|, |\mathcal{O}_i| \propto 1/d$. Since the distribution scales as $p(\mathbf{x}) \propto d^2$ near the node, the resulting estimator can have finite expectation but infinite variance.

To illustrate the resulting pathology, we consider a minimal continuum fermionic system (two spinless fermions on a ring). As shown in Fig. 2(a), the distribution of the energy-gradient estimator exhibits a pronounced heavy tail [80–83]. More precisely, the tail follows $P(|X| > x) \sim Cx^{-\alpha}$ as $x \rightarrow \infty$, with exponent $\alpha \simeq 1.5$. Fig. 2(b) shows that the variance fails to converge with increasing Monte Carlo runs. This behavior is generic. For real (complex) wave functions, the tail exponent of the estimator in Eq. (3) satisfies $\alpha = 3/2$ ($\alpha = 2$), reflecting the codimension of the nodal manifold [52]. Since $\alpha \leq 2$, the variance diverges, leading to anomalously slow and unstable Monte Carlo convergence—the so-called infinite variance problem [52–55], i.e. $\epsilon \propto 1/N^{1/3}$ for $\alpha = 3/2$ and $\epsilon \propto \sqrt{\log(N)}/N$ for $\alpha = 2$ rather than $1/\sqrt{N}$ [82].

Bias in discrete configuration spaces. In discrete configuration spaces, the problem can become more severe. The support of $\psi_\theta(\mathbf{x})$ need not coincide with that of $\langle \mathbf{x} | \hat{H} | \psi_\theta \rangle$, see Fig. 1(c). Configurations that contribute to the exact force may therefore lie outside the sampled support $\text{supp}(\psi_\theta) = \{\mathbf{x} | \psi_\theta(\mathbf{x}) \neq 0\}$. As a result, the Monte Carlo estimator can remain biased even in the infinite-sample limit [56, 57]. Explicitly,

$$F_i - F_i^{\text{MC}} = \frac{\sum_{\mathbf{x} \notin \text{supp}(\psi_\theta)} \langle \partial_i \psi_\theta | \mathbf{x} \rangle \langle \mathbf{x} | \hat{H} | \psi_\theta \rangle}{\sum_{\mathbf{x}} |\psi_\theta(\mathbf{x})|^2}. \quad (4)$$

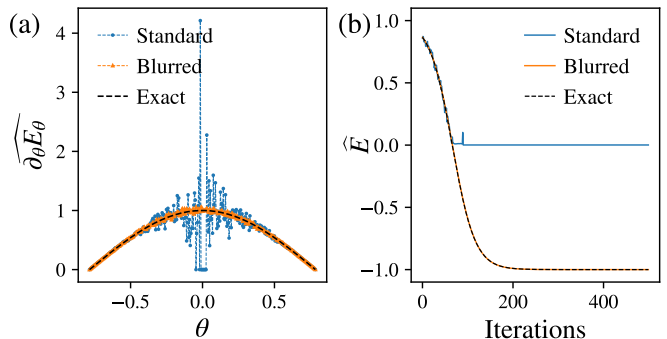


FIG. 3. Pedagogical example in discrete space. We consider a single-spin system with Hamiltonian $\hat{H} = X$ and $\psi_\theta = (\cos(\theta), \sin(\theta))$. (a) Gradient estimator at different θ using 1000 samples. As $\theta \rightarrow 0$, standard sampling exhibits large fluctuations and develops a systematic bias, whereas blurred sampling remains stable. (b) Energy optimization via stochastic reconfiguration (SR), initialized at $\theta = \pi/3$. Standard sampling can become trapped near $\theta \rightarrow 0$, while blurred sampling follows the exact imaginary-time trajectory.

The right-hand side corresponds precisely to the contribution of configurations that are never sampled under p . We refer to this structural discrepancy as a *support-mismatch bias*. Even absent an absolute mismatch, when $\psi_\theta(\mathbf{x}) \ll \langle \mathbf{x} | \hat{H} | \psi_\theta \rangle$ on rarely sampled configurations, the ratio-type structure of the estimator can strongly amplify statistical fluctuations and render the simulation unstable. The effect of the support-mismatch bias is illustrated in Fig. 3, using a single-spin example with $\hat{H} = X$, and variational ansatz $\psi_\theta = (\cos \theta, \sin \theta)$. As $\theta \rightarrow 0$, the gradient estimator exhibits increasingly large fluctuations and eventually develops a systematic bias. As a result, a simple ground state optimization can lead to an incorrect answer. These issues are not specific to the force: the QGT, sharing the same ratio-type structure, is subject to an analogous bias and instabilities.

C. Requirements for a Remedy

The infinite variance problem and support-mismatch bias identified above present a number of challenges, compounded by the fact that VMC is typically applied in extremely high dimensions. A natural strategy for remedying nodes is to modify the sampling distribution via importance sampling [84]. By drawing samples \mathbf{x}' from a reference distribution $r(\mathbf{x}')$, the variational force in Eq. (1) can be evaluated in a self-normalized importance sampling (SNIS) form:

$$F_i^{\text{SNIS}} = \frac{\langle \omega \mathcal{O}_i^* E_{\text{loc}} \rangle_r}{\langle \omega \rangle_r} - \frac{\langle \omega \mathcal{O}_i^* \rangle_r \langle \omega E_{\text{loc}} \rangle_r}{\langle \omega \rangle_r^2}, \quad (5)$$

where $\omega(\mathbf{x}) \equiv p(\mathbf{x})/r(\mathbf{x})$ is the *reweighting factor*. Note that divergences arising from rarely sampled configurations can now be compensated by the reweighting factor

| Method | Infinite variance | Force bias | ESS scaling | Sampling | Additional complexity |
|--|-------------------|------------|--------------|----------------|-----------------------|
| Overdispersed sampling $ \psi_\theta ^\alpha$ [62, 63] | solved | unsolved | $O(e^{-N})$ | modified | 0 |
| E_{loc} regularization [65] | solved | unsolved | $O(1)$ | modified | E_{loc} |
| Node distance regularization [64] | solved | N/A | $O(1)$ | modified | $\nabla\psi_\theta$ |
| Blurred sampling (this work) | solved | solved | $\geq 1 - q$ | postprocessing | 0; N_{conn} |

TABLE I. Comparison between different importance sampling methods and the blurred sampling approach. The ESS scaling refers to how the effective sample size, defined in Eq. (12), scales with the system size N . The additional complexity quantifies the extra computational cost beyond standard sampling, measured in terms of additional wavefunction evaluations, which typically constitute the main computational bottleneck of the algorithm. For the middle two methods, this cost is difficult to express purely in terms of wavefunction evaluations; instead, we list the primary additional quantity required by each method. In discrete space, blurred sampling introduces zero overhead, whereas in the continuum the cost scales as N_{conn} .

ω . In principle, infinite variance can be mitigated if r reduces the effective codimension of nodal set. Similarly, the support-mismatch bias in the discrete case can be resolved provided that the reference distribution satisfies $\text{supp}(\hat{H}\psi_\theta) \cup \text{supp}(\psi_\theta) \subseteq \text{supp}(r)$ for the forces and $\text{supp}(\partial_{\theta_i}\psi_\theta(\mathbf{x})\partial_{\theta_j}\psi_\theta(\mathbf{x})) \cup \text{supp}(\psi_\theta) \subseteq \text{supp}(r)$ for the QGT. In both cases, the missing contributions are restored.

However, identifying a proper choice of $r(\mathbf{x})$ that is easy to sample, removes the nodes, and does not significantly modify the distribution elsewhere is very difficult. Because quantum problems typically involve extremely high-dimensional configuration spaces, $p(\mathbf{x})$ can vary by many tens of orders of magnitude across configurations [53]. This difficulty is further compounded by the fact that modifying the sampling distribution introduces a reweighting factor $\omega = p/r$, whose fluctuations strongly affect the statistical efficiency of the estimator.

Existing approaches construct r in different ways. For example, overdispersed sampling schemes employ $r(\mathbf{x}) \propto |\psi(\mathbf{x})|^\alpha$ with $\alpha < 2$, which broadens the distribution and is straightforward to sample [62, 63]. However, the resulting reweighting factor $\omega \propto |\psi|^{2-\alpha}$ exhibits increasingly large fluctuations as the system size grows, causing an exponential degradation of the effective sample size ($\text{ESS} \equiv \langle \omega \rangle_r^2 / \langle \omega^2 \rangle_r$) and preventing reliable scaling to larger systems. Other methods introduce explicit regularization factors based on local-energy estimators or nodal-distance diagnostics [64, 65], leading to modified distributions of the form $r(\mathbf{x}) = g(\mathbf{x})p(\mathbf{x})$, where $g(\mathbf{x})$ is constructed to diverge near the nodal set so as to compensate for the vanishing of $p(\mathbf{x})$. While such constructions can partially tame divergences, they typically rely on continuum-space diagnostics and substantially alter the target distribution. This increases algorithmic complexity, requires additional evaluations per configuration, and makes the overall computational cost difficult to control, particularly in the context of modern neural-network quantum states (NQS).

These examples illustrate that designing a suitable reference distribution involves balancing several competing objectives. An admissible reference distribution must simultaneously satisfy the following requirements:

(i) it should have sufficiently broad support to regularize nodal singularities;

(ii) it should control the fluctuations of $\omega(\mathbf{x})$ to prevent effective-sample-size collapse;

(iii) it should remain computationally efficient for sampling and evaluation of the reweighting factor.

These requirements are generally in tension with one another, and no existing reference distribution satisfies all of them simultaneously in a generic VMC setting (see Table I).

III. BLURRED SAMPLING METHOD

Overcoming these challenges requires a different strategy. Conceptually inspired by the bridge-link method in determinant quantum Monte Carlo [53, 55], we introduce a local mixing scheme applied to sampled configurations as a post-processing step. This construction, which we term *blurred sampling*, modifies configurations without redefining the underlying sampling distribution. Intuitively, it “blurs” sampled configurations, replacing the singular sampling measure with a locally mixed reference distribution that assigns finite weight near nodal regions. In effect, this produces an effective $r(\mathbf{x})$ that is coupled to $p(\mathbf{x})$ locally, allowing the reweighting factor $\omega(\mathbf{x})$ to remain well behaved as sampling traverses the widely varying landscape of $p(\mathbf{x})$.

A. Construction

Starting from a configuration $\mathbf{x} \sim p(\mathbf{x})$, a new configuration \mathbf{x}' is generated according to a *blur kernel*, defined by the discrete Markov transition kernel

$$K(\mathbf{x}'|\mathbf{x}) = (1 - q)\delta_{\mathbf{x}',\mathbf{x}} + qK_{\text{off}}(\mathbf{x}'|\mathbf{x}), \quad (6)$$

where $0 \leq q < 1$ controls the strength of the blurring. Operationally, with probability $1 - q$ the configuration \mathbf{x} is left unchanged, while with probability q it is updated according to the normalized, off-diagonal kernel $K_{\text{off}}(\mathbf{x}'|\mathbf{x})$, which satisfies $K_{\text{off}}(\mathbf{x}|\mathbf{x}) = 0$ and $\sum_{\mathbf{x}'} K_{\text{off}}(\mathbf{x}'|\mathbf{x}) = 1$ for any \mathbf{x} . This post-processing step induces an implicit reference distribution for \mathbf{x}' ,

$$r(\mathbf{x}') = \sum_{\mathbf{x}} K(\mathbf{x}'|\mathbf{x})p(\mathbf{x}). \quad (7)$$

Because all contributions to $r(\mathbf{x}')$ are nonnegative, we have $r(\mathbf{x}') > 0$ whenever there exists a configuration \mathbf{x} with $K(\mathbf{x}'|\mathbf{x}) > 0$ and $p(\mathbf{x}) > 0$. The blurring operation therefore expands the support of the sampling distribution according to the connectivity structure of $K_{\text{off}}(\mathbf{x}'|\mathbf{x})$, satisfying requirement (i) of Sec. II C, given an appropriately chosen kernel $K(\mathbf{x}'|\mathbf{x})$. The blur kernel can be chosen in a variety of ways; below we present representative constructions for continuum and discrete systems and illustrate their effectiveness using the two pedagogical examples introduced in Sec. II B.

Continuum systems. In continuum space where $\mathbf{x} = \{\vec{r}_1, \dots, \vec{r}_{n_e}\}$, singular behavior arises from the vanishing of the wave function along nodal manifolds. Locally, the wave function varies linearly along normal directions to the nodal set. It therefore suffices to introduce small local perturbations of configurations so as to assign nonzero weight to configurations in the nodal set. To cover all local coordinate directions, one simple way is to define the connected set

$$\mathcal{C}^{\text{out}}(\mathbf{x}) = \{\mathbf{x} \pm \epsilon \mathbf{e}_{i\alpha} | i = 1, \dots, n_e, \alpha = 1, \dots, d\}, \quad (8)$$

where $\mathbf{e}_{i\alpha}$ shifts the α -th coordinate of particle i by one unit and ϵ is a small parameter to control the noise strength. We then use the blur kernel

$$K(\mathbf{x}'|\mathbf{x}) = (1 - q) \delta_{\mathbf{x}',\mathbf{x}} + \frac{q}{N_{\text{conn}}} \sum_{\mathbf{y} \in \mathcal{C}^{\text{out}}(\mathbf{x})} \delta_{\mathbf{x}',\mathbf{y}}, \quad (9)$$

where $N_{\text{conn}} = |\mathcal{C}^{\text{out}}(\mathbf{x})| = 2dn_e$. This means that for each sampled configuration \mathbf{x} , with probability q one particle is randomly displaced by ϵ along one of the coordinate directions. The connectivity therefore remains sparse and scales linearly with system size. Since all dn_e local coordinate directions are covered, the procedure effectively smears nodal singularities (see Fig. 1(b)). For the example shown in Fig. 2, blurred sampling ($q = 2/3$, $\epsilon = 0.2$) straightforwardly eliminates the infinite-variance problem.

Discrete configuration space. In discrete spaces, the bias of the force \mathbf{F} originates from the support mismatch between ψ_θ and $\hat{H}\psi_\theta$. We therefore exploit the connectivity structure of the Hamiltonian to define the blur kernel. Specifically, we denote by

$$\mathcal{C}^{\text{out}}(\mathbf{x}) = \{\mathbf{y} \neq \mathbf{x} | \langle \mathbf{y} | \hat{H} | \mathbf{x} \rangle \neq 0\} \quad (10)$$

the set of configurations connected to \mathbf{x} by \hat{H} , and adopt the same kernel as in Eq. (9). More refined kernels are also possible; for example, the transition probabilities can be weighted according to the matrix elements of \hat{H} .

With this construction, the support-mismatch bias is eliminated for the variational force \mathbf{F} . Since $\text{supp}(\psi_\theta) \cup \text{supp}(\hat{H}\psi_\theta) \subseteq \text{supp}(r)$, all configurations contributing to the force are sampled, and the resulting estimator becomes unbiased. In the example of Fig. 3, blurred sampling ($q = 0.5$) removes both the bias and the large fluctuations of the gradient estimator, leading to stable and smooth ground-state optimization.

B. Statistical Guarantees and Computational Scaling

The blurred sampling method possesses two key statistical properties. First, the reweighting factor satisfies $\langle \omega(\mathbf{x}') \rangle_r = 1$ as a direct consequence of the Markov property (see App. A 1). As a result, the SNIS estimator in Eq. (5) has a standard importance-sampling form, and the following estimator (an analogous expression holds for QGT)

$$\hat{F}_i^{\text{blur}} = \frac{N[\omega]_r^2}{N-1} \times \left(\frac{[\omega \mathcal{O}_i^* E_{\text{loc}}]_r}{[\omega]_r} - \frac{[\omega \mathcal{O}_i^*]_r [\omega E_{\text{loc}}]_r}{[\omega]_r} \right) \quad (11)$$

is finite-sample unbiased, i.e. $\mathbb{E}[\hat{F}_i^{\text{blur}}] = \lim_{N \rightarrow \infty} \hat{F}_i^{\text{blur}}$ (see App. A 2). Here $[\cdot]_r = \frac{1}{N} \sum_{\mathbf{x}'} \cdot(\mathbf{x}')$ denotes the finite-sample average over samples drawn from r . This estimator differs from the SNIS estimator only by an overall factor $\frac{N[\omega]_r^2}{N-1}$. Consequently, in solving the TDVP equation in Eq. (2), this common factor cancels in the linear system. Blurred sampling can therefore be implemented operationally in a self-normalized form while retaining finite-sample unbiasedness.

Second, the fluctuations of $\omega(\mathbf{x}')$ are explicitly controlled. From the construction of the blur kernel in Eq. (6), the reweighting factor is bounded as $0 \leq \omega(\mathbf{x}') \leq 1/(1-q)$. This boundedness immediately implies a lower bound on the effective sample size (ESS) (see App. A 3):

$$\text{ESS}(\omega(\mathbf{x}')) \equiv \frac{\langle \omega(\mathbf{x}') \rangle_r^2}{\langle \omega(\mathbf{x}')^2 \rangle_r} \geq 1 - q. \quad (12)$$

Thus, for any fixed $0 < q < 1$, the effective sample size remains finite, preventing its exponential degradation with increasing system size. Consequently, the blurred sampling method avoids the finite-sample bias inherent to SNIS, and satisfies requirement (ii) outlined in Sec. II C. Importantly, the method is robust to the precise choice of q : for a broad range of $q \sim O(1)$, the estimator remains stable, as will be demonstrated in the numerical results later.

The blurred sampling method also exhibits well-controlled computational cost. The blurring step is a *post-processing* procedure and does not require additional wave-function evaluations; hence, it does not inherit the computational complexity of the underlying ansätze and can therefore be combined seamlessly with sophisticated sampling methods [66, 67] and autoregressive networks [68–74]. The only additional cost, measured in units of wave-function evaluations (the dominant expense in VMC), arises from computing the reweighting factor

$$\omega(\mathbf{x}') = \frac{p(\mathbf{x}')}{(1-q)p(\mathbf{x}') + \sum_{\mathbf{x} \in \mathcal{C}^{\text{in}}(\mathbf{x}')} K(\mathbf{x}'|\mathbf{x})p(\mathbf{x})}, \quad (13)$$

where $\mathcal{C}^{\text{in}}(\mathbf{x}') = \{\mathbf{x} | K(\mathbf{x}'|\mathbf{x}) > 0\}$ denotes the set of configurations connected to \mathbf{x}' through the kernel. Evaluating $\omega(\mathbf{x}')$ therefore requires $|\mathcal{C}^{\text{in}}(\mathbf{x}')|$ wave-function

evaluations. To preserve computational scalability, we restrict the blur kernel to be sparsely connected, such that $|\mathcal{C}^{\text{in}}(\mathbf{x}')|$ grows at most polynomially with system size. Under this constraint, blurred sampling does not alter the overall computational scaling of standard VMC, thereby satisfying requirement (iii) in Sec. II C.

In the continuum case, the kernel introduced above is symmetric and sparsely connected, with $|\mathcal{C}^{\text{in}}(\mathbf{x})| = |\mathcal{C}^{\text{out}}(\mathbf{x})| = 2dn_e$, which scales linearly with system size. In discrete configuration spaces, evaluating the reweighting factor in Eq. (13) requires amplitudes of the wavefunction only on configurations connected by \hat{H} . These amplitudes are already computed in the evaluation of the local energy. Consequently, blurred sampling in the discrete case introduces essentially no additional computational cost.

C. Generalizations

The constructions introduced above rely on a fixed blur kernel with a prescribed connectivity structure. While this deterministic choice suffices to eliminate the dominant pathologies—such as infinite variance and bias in the variational force—there remain situations in which a broader exploration of configuration space may be desirable. One possibility would be to employ more densely connected kernels, with the associated reweighting factor estimated through an auxiliary Monte Carlo procedure [53]. Although such constructions expand the accessible support, they involve an additional stochastic layer (Alternative to the separate Monte Carlo integration, a different computational structure [85] has been explored).

This motivates a randomized generalization of blurred sampling that enlarges the effective support while preserving computational efficiency. Specifically, consider a family of sparse blur kernels $\{K_\lambda\}$ with a connectivity structure that is parameterized by λ , each satisfying the structure of Eq. (6). For each sample $\mathbf{x}_i \sim p(\mathbf{x})$, we independently draw $\lambda_i \sim f(\lambda)$ from a normalized density f , and then generate $\mathbf{x}'_i \sim K_{\lambda_i}(\cdot|\mathbf{x}_i)$. Let $r_\lambda(\mathbf{x}') = \sum_{\mathbf{x}} p(\mathbf{x}) K_\lambda(\mathbf{x}'|\mathbf{x})$ denote the blurred distribution corresponding to a fixed λ . We define the conditional reweighting factor $\omega_\lambda(\mathbf{x}') = \frac{p(\mathbf{x}')}{r_\lambda(\mathbf{x}')}.$

The estimator in Eq. (11) then applies analogously under randomized blurred sampling, with $[\omega \cdot]_r$ replaced by $[\omega_\lambda \cdot]_{f(\lambda)r_\lambda}$. Through the stochastic choice of K_λ , the sampling effectively explores a broader support while preserving finite-sample unbiasedness. Importantly, the weight is evaluated conditionally with respect to the realized kernel K_λ , so the computational cost is controlled by the sparsity of each individual kernel rather than by the averaged kernel. This randomized construction increases flexibility while preserving scalability. As illustrated in later examples, such flexibility can further mitigate instabilities in the QGT and enable more refined blur kernels like a Gaussian kernel in the continuum case. A detailed

derivation of the randomized blurred sampling scheme is provided in Appendix A 4.

In summary, blurred sampling provides a structurally robust solution under the general importance-sampling scheme. Unlike overdispersed or explicitly regularized reference distributions (see Table I), it preserves the underlying sampling dynamics and avoids reweighting factors with system-size-dependent variance growth. Instead, it operates as a sparse post-processing step that restores missing support and regularizes singular estimators while maintaining computational scalability.

IV. RESULTS

Having established the conceptual foundation of blurred sampling and validated it on pedagogical examples, we now turn to time-dependent variational Monte Carlo (t-VMC), where statistical pathologies have been explicitly identified in the literature [56, 86]. In this setting, the correctness of the time evolution hinges directly on the unbiasedness and stability of the Monte Carlo estimators entering the TDVP equation. Thus blurred sampling directly addresses a fundamental limitation in applications of t-VMC for quantum dynamics.

All numerical simulations were performed using NetKet [87, 88]. Small-scale exact benchmarks were obtained with QuTiP [89], while larger-scale benchmarks were computed using the Majorana representation [90, 91]. Further details of the numerical implementation are provided in App. D, and the code required to reproduce all results is available at [92].

A. Illustration with Previously Identified Difficult Examples

We first revisit two benchmarks where standard t-VMC is known to fail due to bias in the force estimators.

(i) *Single spin.* Following Ref. [56], we evolve $|\psi_\theta\rangle = \alpha|0\rangle + \beta|1\rangle$ under $\hat{H} = Y$. As the state approaches $|0\rangle$, standard sampling collapses due to a support-mismatch bias. Blurred sampling removes the bias and reproduces the exact dynamics, as shown in Fig. 4(a).

(ii) *2×2 Heisenberg quench.* We next consider the anisotropic-bond Heisenberg model [86],

$$\hat{H}_{\text{HM}} = \sum_{\langle i,j \rangle} \hat{\mathbf{S}}_i \cdot \hat{\mathbf{S}}_j + \Delta J \sum_{(i,j) \in \text{vert}} \hat{\mathbf{S}}_i \cdot \hat{\mathbf{S}}_j, \quad (14)$$

where the second term runs over the vertical bonds of the lattice. In Ref. [86], it was shown that a complex Restricted Boltzmann Machine (RBM) with a single hidden parameter fails to reproduce the correct real-time dynamics under t-VMC for the 2×2 system. The initial state is taken as the ground state of \hat{H} at $\Delta J = 0$ and is subsequently quenched to $\Delta J = -2$. The correlation $\sum_{(i,j) \in \text{vert}} \langle \hat{\mathbf{S}}_i \cdot \hat{\mathbf{S}}_j \rangle \equiv \langle \hat{\mathbf{S}}_i \cdot \hat{\mathbf{S}}_j \rangle_{\text{vert}}$ is measured as a

function of time. Consistent with their findings, the standard Monte Carlo method breaks down due to support-mismatch bias, whereas blurred sampling successfully restores the correct dynamics, as shown in Fig. 4(b).

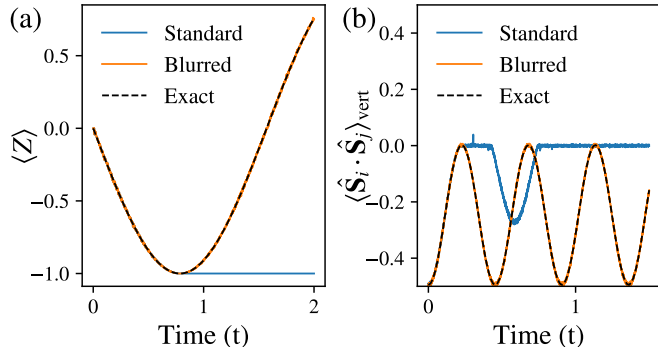


FIG. 4. t-VMC results for two known benchmark problems. (a) We use the variational state $|\psi_\theta\rangle = \alpha|0\rangle + \beta|1\rangle$, with $(\alpha, \beta) = (1, 1)$ at $t = 0$ and evolve it under $U(t) = \exp\{-itY\}$ with t-VMC. As shown in Ref. [56] the standard Monte Carlo estimator collapses due to finite-support bias as the variational state gets close to $|0\rangle$, causing the dynamics to diverge. With blurred sampling, the correct dynamics is recovered. (b) A complex RBM with a single hidden unit fails to provide the correct dynamics under t-VMC for the 2×2 Heisenberg Hamiltonian [86], as the spin correlation diverges from the exact result using the standard sampler. The blurred sampling method produces the correct dynamics. In both cases, we use $q = 0.5$ Hamiltonian-induced kernel for blurred sampling.

B. Solution of the Parity Mixing Problem

We now turn to a larger-scale problem that captures a physically relevant mechanism: symmetry-sector mixing during non-equilibrium dynamics. In many quantum quenches, the initial state that is being evolved may reside entirely within a specific symmetry sector, while the quench Hamiltonian couples different symmetry sectors to each other. The exact time evolution then necessarily involves coherent transfer of weight between them. Accurately describing such sector mixing is essential for capturing dynamical symmetry restoration, collective oscillations, and more generally symmetry-changing processes in non-equilibrium systems.

To construct a setting where this mechanism appears in a controlled manner, we consider an n -site, spin- $\frac{1}{2}$ system initialized in the equal superposition of all configurations $\mathbf{x} \in \{\pm 1\}^n$ with even Z -parity,

$$|\psi_\theta^{\text{even}}\rangle = \sum_{\mathbf{x} \in \mathcal{X}_{\text{even}}} |\mathbf{x}\rangle, \quad (15)$$

where $\mathcal{X}_{\text{even}} = \{\mathbf{x} \in \{\pm 1\}^n : \hat{P}_Z |\mathbf{x}\rangle = +|\mathbf{x}\rangle\}$ and the Z -parity operator is defined as $\hat{P}_Z = \prod_{i=1}^n Z_i$. Here $|\mathbf{x}\rangle$ denotes a computational-basis (Z -basis) state.

The system is evolved under the Hamiltonian of a transverse-field Ising model (TFIM) with periodic boundary condition:

$$\hat{H}_{\text{TFIM}} = J \sum_{i=1}^n Z_i Z_{i+1} + h \sum_{i=1}^n X_i. \quad (16)$$

Crucially, the spin-flip terms in \hat{H}_{TFIM} maps even-parity configurations to odd-parity ones, so that $\hat{H} |\psi_\theta^{\text{even}}\rangle$ has support on $\mathcal{X}_{\text{odd}} = \{\mathbf{x} \in \{\pm 1\}^n : \hat{P}_Z |\mathbf{x}\rangle = -|\mathbf{x}\rangle\}$, while $|\psi_\theta^{\text{even}}\rangle$ itself has support only on $\mathcal{X}_{\text{even}}$. As a consequence, the force estimator becomes systematically biased, since Monte Carlo sampling under $p(\mathbf{x})$ cannot access configurations that carry nonzero weight in $\hat{H}_{\text{TFIM}} |\psi_\theta^{\text{even}}\rangle$.

In Fig. 5, we investigate the dynamics with t-VMC, by computing the time-dependent expectation value of the Z -parity under real-time evolution $U(t) = \exp(-it\hat{H}_{\text{TFIM}})$, starting from $|\psi_\theta^{\text{even}}\rangle$. For the $n = 8$ system, we employ a complex RBM as the variational ansatz. For this architecture, the initial state can be represented analytically (see App. B1) and the full dynamics can be simulated exactly with Majorana fermions (see App. B2). At $t = 0$, the standard Monte Carlo sampling draws configurations only from the even-parity sector. Consequently, the parity remains constant, as evidenced by the flat curve in Fig. 5(a), and the TDVP dynamics is, incorrectly, frozen.

One might expect that initializing the evolution slightly away from the pathological point, i.e., at a small $t_0 > 0$ where the state already contains a small odd-parity component, would restore the correct dynamics. However, we observe that standard sampling still fails: although odd-sector configurations are now formally present, their statistical weight remains extremely small, leading to a severely biased and noisy force estimator. The resulting trajectory deviates from the exact solution at later times as shown in Fig. 5(a).

In contrast, blurred sampling restores access to the missing parity sector at every time step and faithfully reproduces the exact real-time dynamics over long times. Moreover, the results are robust with respect to the blur strength q , which we vary in the range $q \in [0.1, 0.9]$. This demonstrates the stability of the method against changes in its only hyperparameter. We also stress that all previous results presented in this work are similarly insensitive to the choice of q . This robustness stems from the bounded effective sample size and the structural elimination of estimator bias. As shown in Fig. 5(b), the effective sample size remains lower-bounded by $1 - q$, in agreement with the theoretical expectation.

To demonstrate scalability, we extend the system size to $n = 64$ spins. For these larger systems, we find that the RBM ansatz is no longer sufficiently expressive to accurately capture the long time evolution. To disentangle variational expressiveness from estimator bias in the t-VMC algorithm, we instead employ a Gaussian state ansatz tailored to the structure of the problem, which is

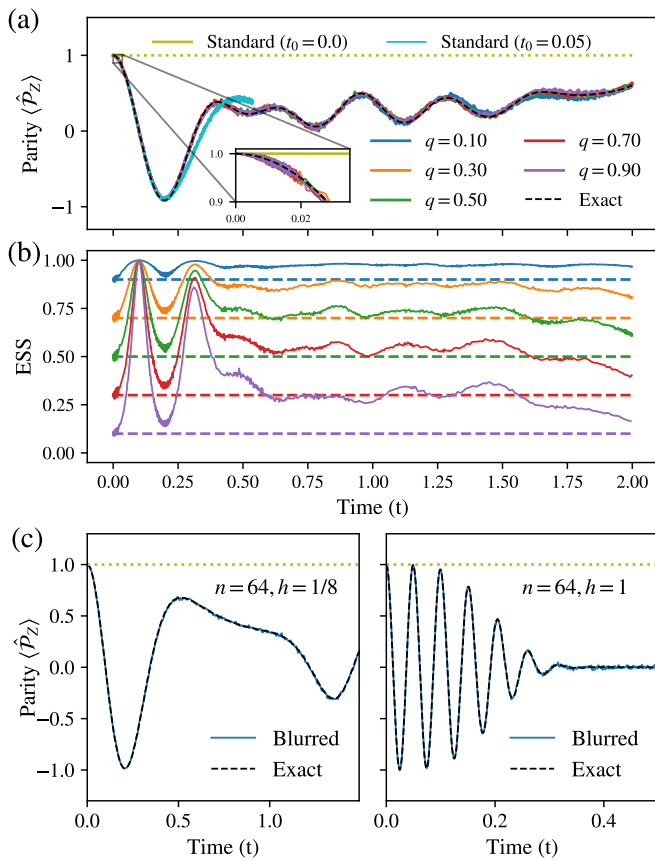


FIG. 5. Accurate simulations of spin parity mixing with blurred sampling in t-VMC. (a) Time evolution of the parity operator for the quench of the 8-spin state $|\psi_{\theta}^{\text{even}}\rangle$ under the TFIM Hamiltonian at $J = h = 1$. The variational state is an RBM with 32 hidden units. Different lines indicate simulations with different values of the blur strength q . The inset shows that starting the t-VMC simulation with the standard estimator at $t_0 = 0$ leads to the immediate freezing of the dynamics due to the bias of the force. The dotted line shows the expected behavior of the parity for the standard $t = 0$ dynamics. If we start the simulation at $t_0 = 0.05$, the standard estimator performs well for the initial ramp of the oscillation, but diverges for longer times. (b) The effective sample size $\text{ESS} = \mathbb{E}[\omega(\mathbf{x}')^2] / \mathbb{E}[\omega(\mathbf{x}')]^2$. The dashed lines indicate the value $1 - q$. At initialization, the ESS is exactly $1 - q$. For all q , the ESS peaks whenever the parity goes through 0, indicating that the state is balanced between odd and even parity sectors. (c) Time evolution of the parity operator using a Gaussian-state ansatz, with $n = 64$. We show the slow ($h = 1/8$) and fast ($h = 1$) quench on the left and right, respectively. The dotted line indicates the expected freezing of the t-VMC dynamics with the standard estimator. Blurred sampling uses the Hamiltonian-induced kernel with $q = 0.5$.

capable of representing the exact state at all times (see App. B3). As shown in Fig. 5(c), blurred sampling accurately reproduces the parity-mixing dynamics for both a slow quench ($h = 1/8$) and a fast quench ($h = 1$), whereas the standard method fails in both cases. This demonstrates that our method remains stable and accu-

rate at large system sizes and across different dynamical regimes.

C. Unbiased Spin Relaxation Dynamics

We now consider a physically distinct regime in which the variational state is initially highly localized in configuration space. Such situations naturally arise in spin-relaxation dynamics, where the system starts from a nearly classical product state and evolves under a many-body Hamiltonian. Strong localization of the wavefunction also appears in neural quantum state simulations of quantum circuits, where one typically evolves a single computational basis state [48]. In all these cases, the state carries significant weight on only a small subset of configurations, and an accurate description of the time evolution requires efficient exploration of the surrounding states in the Hilbert space. They thus provide realistic and stringent tests of the new method in a large class of important applications.

We also use this problem to provide an illustration of how the flexibility of the blurred sampling framework can be exploited to further enlarge the effective sampling support. The Hamiltonian-induced blur ensures that $\text{supp}(\hat{H}\psi_{\theta})$ is sampled and therefore removes the bias in the force estimator. However, the QGT can still suffer from a support mismatch when $\text{supp}(\partial_{\theta_i}\psi_{\theta}(\mathbf{x})\partial_{\theta_j}\psi_{\theta}(\mathbf{x})) \subsetneq \text{supp}(\hat{H}\psi_{\theta}) \cup \text{supp}(\psi_{\theta})$ (see further discussion in App. A5). Note that unlike the bias in the forces, the QGT pathology depends explicitly on the chosen parameterization of the state through the derivatives of the wavefunction.

We adopt a parameterization of our variational ansatz in which a symmetric complex RBM is multiplied with a factor $f_{\phi}(\mathbf{x})$, $\phi \in \mathbb{C}^{n+1}$,

$$\psi_{\theta}(\mathbf{x}) = f_{\phi}(\mathbf{x}) \psi_{\text{symm-RBM}}(\mathbf{x}).$$

Two forms of f_{ϕ} are considered, to help illustrate the effect of the randomized blurred sampling. In the first, different spin sectors are parameterized independently in $f_{\phi}(\mathbf{x}) = \phi_{s(\mathbf{x})}$, while in the second we break the independence, and let $f_{\phi} = \phi_1 + \phi_3$ when $s(\mathbf{x}) = 3$, thereby correlating $s = 1$ to the $s = 3$ spin sectors. (See App. C2 for further details.) Below we refer to the two parameterization schemes as *uncorrelated* and *correlated*, respectively.

The variational state is initialized in the fully polarized all-down product state, with exponentially small amplitudes assigned to all other configurations (see App. C2 for more details). It is straightforward to see that, under the TFIM Hamiltonian ($J=h=1$), the resulting state has significant support mismatch between the QGT estimator and the forces estimator.

We exploit the flexibility of randomized blurred sampling to further enlarge the effective sampling support. We introduce $\lambda = \{s_1, \dots, s_n\}$, $s_i = \pm 1$ as a flip mask, and denote $\lambda \cdot \mathbf{x} = \{x_1 s_1, \dots, x_n s_n\}$ to be the configuration obtained by flipping the spins of \mathbf{x} according to

λ . The flip mask λ is sampled uniformly in different spin sectors. The parameterized blur kernel is defined as

$$K_\lambda(\mathbf{x}'|\mathbf{x}) = (1 - q_1 - q_2)\delta_{\mathbf{x}',\mathbf{x}} + \frac{q_1}{N_{\text{conn}}} \sum_{y \in \mathcal{C}^{\text{out}}(\mathbf{x})} \delta_{\mathbf{x}',y} + q_2 \delta_{\mathbf{x}',\lambda \cdot \mathbf{x}}, \quad (17)$$

where q_1 and q_2 control the strength of two distinct blurring mechanisms: q_1 introduces Hamiltonian-induced blurring as discussed in the previous section; q_2 introduces a flip via the sampled mask λ . For each fixed λ , the support of $r_\lambda = \sum_{\mathbf{x}} K_\lambda(\mathbf{x}'|\mathbf{x})p(\mathbf{x})$ always contains $\text{supp}(\hat{H}\psi_\theta)$, ensuring that the force estimator remains unbiased. The additional flip term effectively enlarges the accessible configuration space. Notice that $q_2 = 0$ recovers the Hamiltonian-induced blurred sampling of the previous section.

As shown in Fig. 6(a,b), the standard estimator fails to reproduce the correct dynamics under \hat{H}_{TFIM} and remains trapped at the initial state. Interestingly, blurred sampling with only the Hamiltonian-induced term ($q_2=0$) already recovers the correct relaxation dynamics in panel (a), with *uncorrelated* parameterization. This is because of the independent parameterization of the different spin sectors. Once a mild regularization is applied to the QGT, the remaining tangent-space directions are sufficiently well-conditioned to yield the correct parameter evolution, even without the additional randomized flips. See App. C3 for a more detailed analysis. In panel (b), with the *correlated* parameterization, the Hamiltonian-induced blur alone ($q_2 = 0$) is no longer sufficient: the early-time dynamics becomes inaccurate due to the incomplete sampling of tangent-space directions. In this case, the inclusion of randomized blurred sampling restores the correct evolution.

V. DISCUSSION AND CONCLUDING REMARKS

In this work, we addressed one of the outstanding problems impeding a broad range of neural network variational calculations in quantum systems, including ground- and excited-states, finite-temperature properties, and imaginary- and real-time dynamics. We introduced a flexible and general framework, blurred sampling, that regularizes both infinite-variance and support-mismatch pathologies in variational Monte Carlo with a simple sampling scheme which is straightforward to implement. By constructing an implicit reference distribution through a one-step local mixing of configurations, blurred sampling overcomes the challenge of establishing an explicit global reference measure and circumvents the competing requirements that limit conventional importance-sampling approaches.

A key feature of blurred sampling is that it operates as a post-processing step. As a result, it preserves the orig-

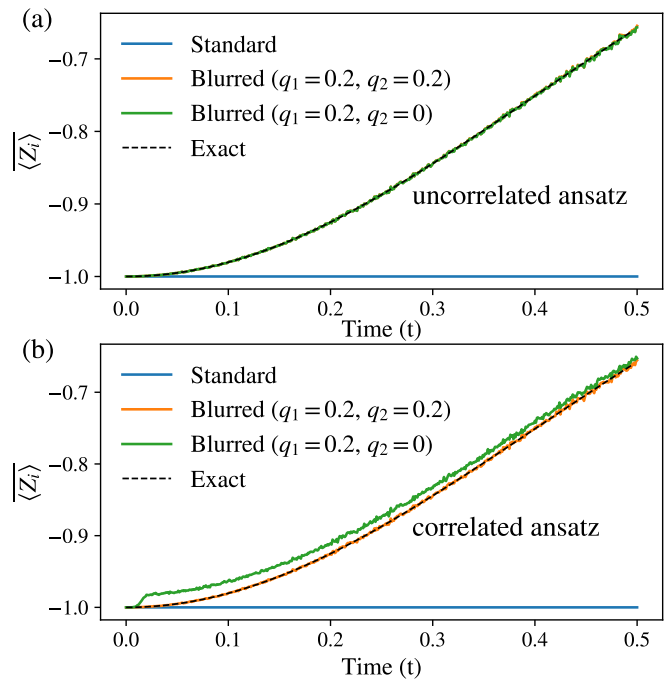


FIG. 6. Solution of the spin relaxation problem. The time evolution of 32 spins in the TFIM ($J = h = 1$) is simulated, initialized in the fully polarized all-down state. The magnetization, defined as the site-averaged expectation value $\langle Z_i \rangle$, is computed as a function of time, and compared against exact results obtained with Majorana fermions (see App. C1). Panels (a) and (b) show the results for two different parameterizations—respectively without and with correlations between parameters across different spin sectors. For standard t-VMC simulations, the dynamics remains trapped in the initial state for both parameterizations, as expected (see also Ref. [56]). In contrast, blurred sampling with only the Hamiltonian-induced blur ($q_2 = 0$) performs well for the uncorrelated parameterization (panel a), but deviates from the exact solution in the correlated case (panel b). Inclusion of randomized blurred sampling (with $q_1, q_2 \neq 0$) successfully captures the relaxation dynamics in both cases.

inal sampling dynamics and autocorrelation structure, making it directly compatible with existing VMC workflows. This distinguishes blurred sampling from methods that rely on modified sampling distributions or additional Markov chains, which can significantly complicate both implementation and analysis.

The generality of the approach suggests several directions for further development. While we focused on simple, physically motivated blur kernels, the framework readily accommodates alternative choices, including problem-specific kernels or adaptive constructions that optimize statistical efficiency. For example, the blurring strength q provides a tunable parameter that interpolates between conventional sampling and fully blurred estimates. More tailored q choices, even including local dependence, can also be engineered to further facilitate ergodicity and increase sampling efficiency.

Although our numerical results focused on t-VMC ap-

plications in quantum dynamics, where the bias in the force estimation has been a major impediment for accurate numerical simulations, it will also be fruitful to study how the bias in the forces and QGT affects ground state optimization problems, which can suffer from slow convergence near the ground state. With the rapid growth of neural quantum state variational calculations, the potential gain in optimization effectiveness and efficiency can impact many applications across physics and chemistry.

Finally, although our analysis has been restricted to variational Monte Carlo, the underlying idea of implicit importance sampling through local configuration mixing is applicable more broadly. Potential extensions include projector quantum Monte Carlo methods, finite-temperature simulations, and classical Monte Carlo problems involving heavy-tailed observables. Exploring these

directions can provide a unified perspective on variance regularization across a wide range of stochastic simulation techniques. It is also of interest to examine the applicability of this approach to other optimization problems in machine learning and related areas of artificial intelligence.

ACKNOWLEDGMENTS

ZW is grateful for discussions with Miguel A. Morales, Conor Smith, Markus Holzmann, and especially thanks Ao Chen for insightful discussions on the lattice model simulations. RW would like to thank Filippo Vicentini and Anka van der Walle for discussions. The Flatiron Institute is a division of the Simons Foundation.

-
- [1] W. L. McMillan, Ground state of liquid he^4 , *Phys. Rev.* **138**, A442 (1965).
 - [2] D. M. Ceperley and B. J. Alder, Ground state of the electron gas by a stochastic method, *Phys. Rev. Lett.* **45**, 566 (1980).
 - [3] G. Carleo and M. Troyer, Solving the quantum many-body problem with artificial neural networks, *Science* **355**, 602 (2017).
 - [4] K. Choo, G. Carleo, N. Regnault, and T. Neupert, Symmetries and many-body excitations with neural-network quantum states, *Phys. Rev. Lett.* **121**, 167204 (2018).
 - [5] S. Pathak, B. Busemeyer, J. N. B. Rodrigues, and L. K. Wagner, Excited states in variational monte carlo using a penalty method, *The Journal of Chemical Physics* **154**, 034101 (2021).
 - [6] M. T. Entwistle, Z. Schätzle, P. A. Erdman, J. Hermann, and F. Noé, Electronic excited states in deep variational monte carlo, *Nature Communications* **14**, 274 (2023).
 - [7] H. Lange, F. Döschl, J. Carrasquilla, and A. Bohrdt, Neural network approach to quasiparticle dispersions in doped antiferromagnets, *Communications Physics* **7**, 187 (2024).
 - [8] G. Carleo, F. Becca, L. Sanchez-Palencia, S. Sorella, and M. Fabrizio, Light-cone effect and supersonic correlations in one- and two-dimensional bosonic superfluids, *Phys. Rev. A* **89**, 031602 (2014).
 - [9] M. Schmitt and M. Heyl, Quantum many-body dynamics in two dimensions with artificial neural networks, *Phys. Rev. Lett.* **125**, 100503 (2020).
 - [10] I. L. Gutiérrez and C. B. Mendl, Real time evolution with neural-network quantum states, *Quantum* **6**, 627 (2022).
 - [11] M. Schmitt, M. M. Rams, J. Dziarmaga, M. Heyl, and W. H. Zurek, Quantum phase transition dynamics in the two-dimensional transverse-field ising model, *Science Advances* **8**, eabl6850 (2022).
 - [12] M. Schmitt and M. Heyl, *Simulating dynamics of correlated matter with neural quantum states* (2025), [arXiv:2506.03124 \[quant-ph\]](https://arxiv.org/abs/2506.03124).
 - [13] S. Sorella, Green function monte carlo with stochastic reconfiguration, *Phys. Rev. Lett.* **80**, 4558 (1998).
 - [14] N. Irikura and H. Saito, Neural-network quantum states at finite temperature, *Phys. Rev. Res.* **2**, 013284 (2020).
 - [15] H. Xie, Z.-H. Li, H. Wang, L. Zhang, and L. Wang, Deep variational free energy approach to dense hydrogen, *Phys. Rev. Lett.* **131**, 126501 (2023).
 - [16] J. Nys, Z. Denis, and G. Carleo, Real-time quantum dynamics of thermal states with neural thermofields, *Phys. Rev. B* **109**, 235120 (2024).
 - [17] J. Nys and J. Carrasquilla, *Fermionic neural gibbs states* (2025), [arXiv:2512.04663 \[quant-ph\]](https://arxiv.org/abs/2512.04663).
 - [18] D. Luo and B. K. Clark, Backflow transformations via neural networks for quantum many-body wave functions, *Phys. Rev. Lett.* **122**, 226401 (2019).
 - [19] Y. Nomura and M. Imada, Dirac-type nodal spin liquid revealed by refined quantum many-body solver using neural-network wave function, correlation ratio, and level spectroscopy, *Phys. Rev. X* **11**, 031034 (2021).
 - [20] W.-Y. Liu, Y.-Z. Huang, S.-S. Gong, and Z.-C. Gu, Accurate simulation for finite projected entangled pair states in two dimensions, *Phys. Rev. B* **103**, 235155 (2021).
 - [21] J. R. Moreno, G. Carleo, A. Georges, and J. Stokes, Fermionic wave functions from neural-network constrained hidden states, *Proceedings of the National Academy of Sciences* **119**, e2122059119 (2022).
 - [22] M. Medvidović and J. R. Moreno, Neural-network quantum states for many-body physics, *The European Physical Journal Plus* **139**, 1 (2024).
 - [23] A. Chen and M. Heyl, Empowering deep neural quantum states through efficient optimization, *Nature Physics* **20**, 1476 (2024).
 - [24] H. Lange, A. Van de Walle, A. Abedinnia, and A. Bohrdt, From architectures to applications: a review of neural quantum states, *Quantum Science and Technology* **9**, 040501 (2024).
 - [25] Y. Gu, W. Li, H. Lin, B. Zhan, R. Li, Y. Huang, D. He, Y. Wu, T. Xiang, M. Qin, L. Wang, and D. Lv, *Solving the hubbard model with neural quantum states* (2025), [arXiv:2507.02644 \[cond-mat.str-el\]](https://arxiv.org/abs/2507.02644).
 - [26] W.-Y. Liu, H. Zhai, R. Peng, Z.-C. Gu, and G. K.-L. Chan, Accurate simulation of the hubbard model with finite fermionic projected entangled pair states, *Phys. Rev. Lett.* **134**, 256502 (2025).
 - [27] A. Chen, Z.-Q. Wan, A. Sengupta, A. Georges, and C. Roth, *Neural network-augmented pfaffian wave-*

- functions for scalable simulations of interacting fermions (2025), [arXiv:2507.10705 \[cond-mat.str-el\]](#).
- [28] X. Li, Y. Chen, B. Li, H. Chen, F. Wu, J. Chen, and W. Ren, [Deep learning sheds light on integer and fractional topological insulators](#) (2025), [arXiv:2503.11756 \[cond-mat.str-el\]](#).
- [29] L. L. Viteritti, R. Rende, S. Sachdev, and G. Carleo, [Approaching the thermodynamic limit with neural-network quantum states](#) (2026), [arXiv:2602.02665 \[cond-mat.str-el\]](#).
- [30] J. Hermann, Z. Schätzle, and F. Noé, Deep-neural-network solution of the electronic schrödinger equation, [Nature Chemistry](#) **12**, 891 (2020).
- [31] D. Pfau, J. S. Spencer, A. G. D. G. Matthews, and W. M. C. Foulkes, Ab initio solution of the many-electron schrödinger equation with deep neural networks, [Phys. Rev. Res.](#) **2**, 033429 (2020).
- [32] K. Choo, A. Mezzacapo, and G. Carleo, Fermionic neural-network states for ab-initio electronic structure, [Nature communications](#) **11**, 2368 (2020).
- [33] J. Hermann, J. Spencer, K. Choo, A. Mezzacapo, W. M. C. Foulkes, D. Pfau, G. Carleo, and F. Noé, Ab initio quantum chemistry with neural-network wavefunctions, [Nature Reviews Chemistry](#) **7**, 692 (2023).
- [34] I. von Glehn, J. S. Spencer, and D. Pfau, [A self-attention ansatz for ab-initio quantum chemistry](#) (2023), [arXiv:2211.13672 \[physics.chem-ph\]](#).
- [35] H. Shang, C. Guo, Y. Wu, Z. Li, and J. Yang, [Solving schrödinger equation with a language model](#) (2024), [arXiv:2307.09343 \[quant-ph\]](#).
- [36] D. Pfau, S. Axelrod, H. Sutterud, I. von Glehn, and J. S. Spencer, Accurate computation of quantum excited states with neural networks, [Science](#) **385**, eadn0137 (2024).
- [37] J. Kim, G. Pescia, B. Fore, J. Nys, G. Carleo, S. Gandolfi, M. Hjorth-Jensen, and A. Lovato, Neural-network quantum states for ultra-cold fermi gases, [Communications Physics](#) **7**, 148 (2024).
- [38] M. Wilson, S. Moroni, M. Holzmann, N. Gao, F. Wudarski, T. Vegge, and A. Bhowmik, Neural network ansatz for periodic wave functions and the homogeneous electron gas, [Phys. Rev. B](#) **107**, 235139 (2023).
- [39] G. Cassella, H. Sutterud, S. Azadi, N. D. Drummond, D. Pfau, J. S. Spencer, and W. M. C. Foulkes, Discovering quantum phase transitions with fermionic neural networks, [Phys. Rev. Lett.](#) **130**, 036401 (2023).
- [40] C. Smith, Y. Chen, R. Levy, Y. Yang, M. A. Morales, and S. Zhang, Unified variational approach description of ground-state phases of the two-dimensional electron gas, [Phys. Rev. Lett.](#) **133**, 266504 (2024).
- [41] G. Pescia, J. Nys, J. Kim, A. Lovato, and G. Carleo, Message-passing neural quantum states for the homogeneous electron gas, [Phys. Rev. B](#) **110**, 035108 (2024).
- [42] M. Geier, K. Nazaryan, T. Zaklama, and L. Fu, Self-attention neural network for solving correlated electron problems in solids, [Phys. Rev. B](#) **112**, 045119 (2025).
- [43] Y. Teng, D. D. Dai, and L. Fu, Solving the fractional quantum hall problem with self-attention neural network, [Phys. Rev. B](#) **111**, 205117 (2025).
- [44] Y. Qian, T. Zhao, J. Zhang, T. Xiang, X. Li, and J. Chen, Describing landau level mixing in fractional quantum hall states with deep learning, [Phys. Rev. Lett.](#) **134**, 176503 (2025).
- [45] C.-T. Li, T. Ong, M. Geier, H. Lin, and L. Fu, [Attention is all you need to solve chiral superconductivity](#) (2025), [arXiv:2509.03683 \[cond-mat.supr-con\]](#).
- [46] Z. Ge, C. Smith, Z. He, Y. Yang, Q. Li, Z. Xiang, J. Xiao, W. Zhou, S. Kahn, M. Erdi, R. Banerjee, T. Taniguchi, K. Watanabe, S. A. Tongay, M. A. Morales, S. Zhang, F. Wang, and M. F. Crommie, [Visualizing the impact of quenched disorder on 2d electron wigner solids](#) (2025), [arXiv:2510.12009 \[cond-mat.str-el\]](#).
- [47] C. Smith, Y. Yang, Z.-Q. Wan, Y. Chen, M. A. Morales, and S. Zhang, [Neural network discovery of paired wigner crystals in artificial graphene](#) (2026), [arXiv:2602.16798 \[quant-ph\]](#).
- [48] M. Medvidović and G. Carleo, Classical variational simulation of the quantum approximate optimization algorithm, [npj Quantum Information](#) **7**, 101 (2021).
- [49] A. D. King, A. Nocera, M. M. Rams, J. Dziarmaga, R. Wiersema, W. Bernoudy, J. Raymond, N. Kaushal, N. Heinsdorf, R. Harris, *et al.*, Beyond-classical computation in quantum simulation, [Science](#) **388**, 199 (2025).
- [50] R. Haghshenas, E. Chertkov, M. Mills, W. Kadow, S.-H. Lin, Y.-H. Chen, C. Cade, I. Niesen, T. Begusić, M. S. Rudolph, *et al.*, [Digital quantum magnetism at the frontier of classical simulations](#) (2025), [arXiv:2503.20870 \[quant-ph\]](#).
- [51] S. Sorella, Generalized lanczos algorithm for variational quantum monte carlo, [Phys. Rev. B](#) **64**, 024512 (2001).
- [52] J. R. Trail, Heavy-tailed random error in quantum monte carlo, [Phys. Rev. E](#) **77**, 016703 (2008).
- [53] H. Shi and S. Zhang, Infinite variance in fermion quantum monte carlo calculations, [Phys. Rev. E](#) **93**, 033303 (2016).
- [54] P. L. Ríos and G. J. Conduit, Tail-regression estimator for heavy-tailed distributions of known tail indices and its application to continuum quantum monte carlo data, [Phys. Rev. E](#) **99**, 063312 (2019).
- [55] Z.-Q. Wan and S. Zhang, Addressing the infinite variance problem in fermionic monte carlo simulations: Retrospective error remediation and the exact bridge link method, [Phys. Rev. E](#) **112**, 065309 (2025).
- [56] A. Sinibaldi, C. Giuliani, G. Carleo, and F. Vicentini, Unbiasing time-dependent Variational Monte Carlo by projected quantum evolution, [Quantum](#) **7**, 1131 (2023).
- [57] D. Hofmann, G. Fabiani, J. H. Mentink, G. Carleo, and M. A. Sentef, Role of stochastic noise and generalization error in the time propagation of neural-network quantum states, [SciPost Phys.](#) **12**, 165 (2022).
- [58] S. Pathak and L. K. Wagner, A light weight regularization for wave function parameter gradients in quantum monte carlo, [AIP Advances](#) **10**, 085213 (2020).
- [59] L. Gravina, V. Savona, and F. Vicentini, Neural projected quantum dynamics: a systematic study, [Quantum](#) **9**, 1803 (2025).
- [60] P. J. Robinson, S. D. Pineda Flores, and E. Neuscamman, Excitation variance matching with limited configuration interaction expansions in variational monte carlo, [The Journal of Chemical Physics](#) **147**, 164114 (2017).
- [61] L. Otis, I. M. Craig, and E. Neuscamman, A hybrid approach to excited-state-specific variational monte carlo and doubly excited states, [The Journal of Chemical Physics](#) **153**, 234105 (2020).
- [62] K. Inui, Y. Kato, and Y. Motome, Determinant-free fermionic wave function using feed-forward neural networks, [Phys. Rev. Res.](#) **3**, 043126 (2021).
- [63] A. Misery, L. Gravina, A. Santini, and F. Vicentini, [Look-](#)

- ing elsewhere: improving variational monte carlo gradients by importance sampling (2025), [arXiv:2507.05352 \[quant-ph\]](#).
- [64] C. Attaccalite and S. Sorella, Stable liquid hydrogen at high pressure by a novel ab initio molecular-dynamics calculation, *Phys. Rev. Lett.* **100**, 114501 (2008).
- [65] J. R. Trail, Alternative sampling for variational quantum monte carlo, *Phys. Rev. E* **77**, 016704 (2008).
- [66] A. Malyshev, M. Schmitt, and A. I. Lvovsky, *Neural quantum states and peaked molecular wave functions: Curse or blessing?* (2024), [arXiv:2408.07625 \[quant-ph\]](#).
- [67] A.-J. Liu and B. K. Clark, *Efficient optimization of neural network backflow for ab-initio quantum chemistry* (2025), [arXiv:2502.18843 \[physics.chem-ph\]](#).
- [68] B. Uria, M.-A. Côté, K. Gregor, I. Murray, and H. Larochelle, Neural autoregressive distribution estimation, *Journal of Machine Learning Research* **17**, 1 (2016).
- [69] M. Hibat-Allah, M. Ganahl, L. E. Hayward, R. G. Melko, and J. Carrasquilla, Recurrent neural network wave functions, *Phys. Rev. Res.* **2**, 023358 (2020).
- [70] O. Sharir, Y. Levine, N. Wies, G. Carleo, and A. Shashua, Deep autoregressive models for the efficient variational simulation of many-body quantum systems, *Phys. Rev. Lett.* **124**, 020503 (2020).
- [71] S. Humeniuk, Y. Wan, and L. Wang, Autoregressive neural Slater-Jastrow ansatz for variational Monte Carlo simulation, *SciPost Phys.* **14**, 171 (2023).
- [72] K. Sprague and S. Czischek, Variational monte carlo with large patched transformers, *Communications Physics* **7**, 90 (2024).
- [73] M. S. Moss, R. Wiersema, M. Hibat-Allah, J. Carrasquilla, and R. G. Melko, Leveraging recurrence in neural network wavefunctions for large-scale simulations of heisenberg antiferromagnets on the square lattice, *Phys. Rev. B* **112**, 134450 (2025).
- [74] M. S. Moss, R. Wiersema, M. Hibat-Allah, J. Carrasquilla, and R. G. Melko, Leveraging recurrence in neural network wavefunctions for large-scale simulations of heisenberg antiferromagnets on the triangular lattice, *Phys. Rev. B* **112**, 134449 (2025).
- [75] G. Carleo, F. Becca, M. Schiró, and M. Fabrizio, Localization and glassy dynamics of many-body quantum systems, *Scientific reports* **2**, 243 (2012).
- [76] D. M. Ceperley, Fermion nodes, *Journal of statistical physics* **63**, 1237 (1991).
- [77] W. M. C. Foulkes, L. Mitas, R. J. Needs, and G. Rajagopal, Quantum monte carlo simulations of solids, *Rev. Mod. Phys.* **73**, 33 (2001).
- [78] L. Mitas, Structure of fermion nodes and nodal cells, *Phys. Rev. Lett.* **96**, 240402 (2006).
- [79] R. J. Needs, M. D. Towler, N. D. Drummond, and P. L. Ríos, Continuum variational and diffusion quantum monte carlo calculations, *Journal of Physics: Condensed Matter* **22**, 023201 (2009).
- [80] P. Lévy, *Calcul des probabilités* (Gauthier-Villars, 1925).
- [81] B. Gnedenko and A. Kolmogorov, *Limit Distributions for Sums of Independent Random Variables*, Addison-Wesley Mathematical Series (Addison-Wesley, 1954).
- [82] J. Nolan, *Univariate Stable Distributions: Models for Heavy Tailed Data*, Springer Series in Operations Research and Financial Engineering (Springer International Publishing, 2020).
- [83] J.-P. Bouchaud and A. Georges, Anomalous diffusion in disordered media: statistical mechanisms, models and physical applications, *Physics reports* **195**, 127 (1990).
- [84] R. Y. Rubinstein, *Simulation and the Monte Carlo Method* (Wiley, 1981).
- [85] A. Alexandru, P. F. Bedaque, A. Carosso, and H. Oh, Infinite variance problem in fermion models, *Phys. Rev. D* **107**, 094502 (2023).
- [86] H. Vrcan and J. H. Mentink, *Instability of explicit time integration for strongly quenched dynamics with neural quantum states* (2025), [arXiv:2507.17421 \[quant-ph\]](#).
- [87] G. Carleo, K. Choo, D. Hofmann, J. E. Smith, T. Westerhout, F. Alet, E. J. Davis, S. Efthymiou, I. Glasser, S.-H. Lin, M. Mauri, G. Mazzola, C. B. Pereira, and F. Vicentini, Netket: A machine learning toolkit for many-body quantum systems, *SoftwareX* **10**, 100311 (2019).
- [88] F. Vicentini, D. Hofmann, A. Szabó, D. Wu, C. Roth, C. Giuliani, G. Pescia, J. Nys, V. Vargas-Calderón, N. Astrakhantsev, and G. Carleo, Netket 3: Machine learning toolbox for many-body quantum systems, *SciPost Phys. Codebases* , 7 (2022).
- [89] Lambert, Neill and Giguère, Eric and Menczel, Paul and Li, Boxi and Hopf, Patrick and Suárez, Gerardo and Gali, Marc and Lishman, Jake and Gadhvi, Rushiraj and Agarwal, Rochisha and Galicia, Asier and Shammah, Nathan and Nation, Paul and Johansson, J. R. and Ahmed, Shah Nawaz and Cross, Simon and Pitchford, Alexander and Nori, Franco , Qutip 5: The quantum toolbox in Python, *Physics Reports* **1153**, 1 (2026).
- [90] Z.-Y. Han, Z.-Q. Wan, and H. Yao, *Pfaffian quantum monte carlo: solution to majorana sign ambiguity and applications* (2024), [arXiv:2408.10311 \[cond-mat.str-el\]](#).
- [91] Z.-Q. Wan, X.-D. Dai, and G.-Y. Zhu, *Revisiting nishimori multicriticality through the lens of information measures* (2025), [arXiv:2511.02907 \[cond-mat.stat-mech\]](#).
- [92] https://github.com/therooler/nqs_blurred_sampling.
- [93] R. Wiersema, Jaxmg: A multi-gpu linear solver in jax (2026), [arXiv:2601.14466 \[cs.DC\]](#).
- [94] M. Solinas, A. Valenti, N. Bou-Rabee, and R. Wiersema, *Neural quantum states in mixed precision* (2026), [arXiv:2601.20782 \[quant-ph\]](#).

Appendix A: Detailed derivation and properties of blurred sampling

In this section, we derive the blurred sampling procedure and prove the properties stated in the main text. Blurred sampling does not modify the original sampler, which generates configurations \mathbf{x} distributed according to $p(\mathbf{x})$. Throughout this section, we denote by \mathbf{x} samples drawn from p , and by \mathbf{x}' the configuration obtained after the post-processing step.

1. Unit expectation of the reweighting factor

We first verify that the reweighting factors have unit expectation, i.e., $\langle \omega(\mathbf{x}') \rangle_r = 1$, for the general blur kernel defined in Eq. (6). Since $K(\mathbf{x}'|\mathbf{x})$ is a Markov kernel, $\sum_{\mathbf{x}'} r(\mathbf{x}') = \sum_{\mathbf{x}'} \sum_{\mathbf{x}} K(\mathbf{x}', \mathbf{x}) p(\mathbf{x}) = \sum_{\mathbf{x}} p(\mathbf{x})$, and hence r is normalized whenever p is normalized. The reweighting factor is defined as $\omega(\mathbf{x}') = p(\mathbf{x}')/r(\mathbf{x}')$. Therefore,

$$\langle \omega(\mathbf{x}') \rangle_r = \sum_{\mathbf{x}'} r(\mathbf{x}') p(\mathbf{x}') / r(\mathbf{x}') = \sum_{\mathbf{x}'} p(\mathbf{x}') = 1. \quad (\text{A1})$$

2. Finite-sample unbiased estimators

We first construct the finite-sample unbiased estimator for expectation values under the original distribution p . Since $\langle \omega \rangle_r = 1$, we have

$$\langle A \rangle_p = \frac{\langle \omega A \rangle_r}{\langle \omega \rangle_r} = \langle \omega A \rangle_r. \quad (\text{A2})$$

Therefore, the finite size estimator

$$\widehat{\langle A \rangle}_p = \frac{1}{N} \sum_{i=1}^N \omega(\mathbf{x}'_i) A(\mathbf{x}'_i) \equiv [\omega A]_r \quad (\text{A3})$$

is an unbiased estimator for $\langle A \rangle_p$ with $\mathbb{E}[\widehat{\langle A \rangle}_p] = \langle A \rangle_p$.

For covariance-type quantities $\langle\langle A, B \rangle\rangle_p \equiv \langle AB \rangle_p - \langle A \rangle_p \langle B \rangle_p$, we use the identities $\langle AB \rangle_p = \langle \omega AB \rangle_r$, $\langle A \rangle_p = \langle \omega A \rangle_r$, $\langle B \rangle_p = \langle \omega B \rangle_r$. Hence,

$$\langle\langle A, B \rangle\rangle_p = \langle \omega AB \rangle_r - \langle \omega A \rangle_r \langle \omega B \rangle_r \quad (\text{A4})$$

We now use the identity $\langle \omega \rangle_r = 1$ to rewrite the first term as $\langle \omega AB \rangle_r = \langle \omega \rangle_r \langle \omega AB \rangle_r$, and add–subtract $\langle \omega^2 AB \rangle_r$:

$$\begin{aligned} \langle\langle A, B \rangle\rangle_p &= \langle \omega \rangle_r \langle \omega AB \rangle_r - \langle \omega^2 AB \rangle_r \\ &\quad - \langle \omega A \rangle_r \langle \omega B \rangle_r + \langle \omega^2 AB \rangle_r \\ &= \langle\langle \omega A, \omega B \rangle\rangle_r - \langle\langle \omega, \omega AB \rangle\rangle_r. \end{aligned} \quad (\text{A5})$$

It is well known that the finite-sample unbiased estimator of the covariance $\langle\langle X_1, X_2 \rangle\rangle_r$ is

$$\langle\langle \widehat{X}_1, \widehat{X}_2 \rangle\rangle_r = \frac{N}{N-1} ([X_1 X_2]_r - [X_1]_r [X_2]_r). \quad (\text{A6})$$

Therefore we have that

$$\begin{aligned} \langle\langle \widehat{A}, \widehat{B} \rangle\rangle_p &= \langle\langle \widehat{\omega A}, \widehat{\omega B} \rangle\rangle_r - \langle\langle \widehat{\omega}, \widehat{\omega AB} \rangle\rangle_r \\ &= \frac{N}{N-1} \times ([\omega]_r [\omega AB]_r - [\omega A]_r [\omega B]_r) \\ &= \frac{N}{N-1} \frac{[\omega]_r^2}{[\omega]_r} \times \left(\frac{[\omega AB]_r}{[\omega]_r} - \frac{[\omega A]_r}{[\omega]_r} \frac{[\omega B]_r}{[\omega]_r} \right), \end{aligned} \quad (\text{A7})$$

is the finite-sample unbiased estimator for $\langle\langle A, B \rangle\rangle_p$.

In practice, one typically employs the self-normalized estimator (i.e., the right-hand side of the last line in Eq. (A7)), which is a biased estimator. However, this bias manifests itself as a common multiplicative factor affecting all covariance-like quantities. Since the SR/TDVP update depends only on ratios of such quantities (e.g., through $\mathbf{S}^{-1}\mathbf{F}$), this common factor cancels in the parameter update. Consequently, the resulting time evolution is unaffected by this overall factor.

3. Bound of the reweighting factor and effective sample size

Consider the distribution obtained after marginalizing the kernel K in Eq. (6):

$$\begin{aligned} r(\mathbf{x}') &= \sum_{\mathbf{x}} K(\mathbf{x}'|\mathbf{x})p(\mathbf{x}) \\ &= \sum_{\mathbf{x}} ((1-q)\delta_{\mathbf{x}',\mathbf{x}}p(\mathbf{x}) + qK_{\text{off}}(\mathbf{x}'|\mathbf{x})p(\mathbf{x})) \\ &= (1-q)p(\mathbf{x}') + q \sum_{\mathbf{x}} K_{\text{off}}(\mathbf{x}'|\mathbf{x})p(\mathbf{x}). \end{aligned} \quad (\text{A8})$$

Since $K_{\text{off}}(\mathbf{x}'|\mathbf{x})p(\mathbf{x}) \geq 0$, we see that

$$r(\mathbf{x}') \geq (1-q)p(\mathbf{x}'). \quad (\text{A9})$$

As a result, the reweighting factor is bounded by

$$\omega(\mathbf{x}') = \frac{p(\mathbf{x}')}{r(\mathbf{x}')} \leq \frac{p(\mathbf{x}')}{(1-q)p(\mathbf{x}')} = \frac{1}{1-q}. \quad (\text{A10})$$

Using the fact that $p(\mathbf{x}') \geq 0$, we conclude that the reweighting factor is bounded as

$$0 \leq \omega(\mathbf{x}') \leq \frac{1}{1-q}. \quad (\text{A11})$$

Since the reweighting factors satisfy $\omega(\mathbf{x}) \in [0, \frac{1}{1-q}]$, we have the pointwise inequality

$$\omega(\mathbf{x})^2 \leq \frac{1}{1-q}\omega(\mathbf{x}). \quad (\text{A12})$$

Taking expectations with respect to r yields

$$\langle \omega^2(\mathbf{x}') \rangle_r \leq \frac{1}{1-q} \langle \omega(\mathbf{x}') \rangle_r. \quad (\text{A13})$$

Using $\langle \omega(\mathbf{x}') \rangle_r = 1$, we obtain

$$\text{ESS}[\omega] = \langle \omega(\mathbf{x}') \rangle_r^2 / \langle \omega(\mathbf{x}')^2 \rangle_r \geq 1 - q. \quad (\text{A14})$$

4. Randomized blur construction

For the randomized generalization of blurred sampling, we first recall the construction. Let K_λ be a family of blur kernels parameterized by λ , where each kernel satisfies the structure of Eq. (6) and has sparse connectivity. For each sample $\mathbf{x}_i \sim p(\mathbf{x})$, we independently draw $\lambda_i \sim f(\lambda)$ from a normalized density f , and then generate $\mathbf{x}'_i \sim K_{\lambda_i}(\cdot|\mathbf{x}_i)$. Let $r_\lambda(\mathbf{x}') = \sum_{\mathbf{x}} p(\mathbf{x})K_\lambda(\mathbf{x}'|\mathbf{x})$ denote the blurred distribution corresponding to a fixed λ . We define the conditional reweighting factor $\omega_\lambda(\mathbf{x}') = \frac{p(\mathbf{x}')}{r_\lambda(\mathbf{x}')}$. Then the estimator $[\omega_\lambda A]_{f(\lambda)r_\lambda}$ remains finite-sample unbiased and equal to $\langle A \rangle_p$,

$$\langle A(\mathbf{x}) \rangle_p = \langle \langle \omega_\lambda(\mathbf{x}')A(\mathbf{x}') \rangle_{r_\lambda} \rangle_{f(\lambda)} = \langle \omega_\lambda(\mathbf{x}')A(\mathbf{x}') \rangle_{f(\lambda)r_\lambda}, \quad (\text{A15})$$

provided that no support-mismatch pathology occurs. Similarly, the estimator in Eq. (11) also applies under randomized blurred sampling, with $[\omega]_r$ replaced by $[\omega_\lambda]_{f(\lambda)r_\lambda(\mathbf{x}')}$. As a direct application, the probabilistic blur construction can be used to refine the continuum kernel introduced in Eq. (8), where the displacement magnitude ϵ and coordinate directions \mathbf{e}_α are treated as random parameters λ . By sampling these quantities from suitable distributions, the resulting blur approaches an effective Gaussian kernel. In particular, this randomization restores rotational symmetry at the level of the induced proposal distribution.

5. QGT estimator from randomized blurred sampling

Although the marginal distribution of \mathbf{x}' is $r(\mathbf{x}') = \sum_{\lambda} f(\lambda) r_{\lambda}(\mathbf{x}')$, which coincides with that induced by the average kernel $K_{\text{mix}}(\mathbf{x}'|\mathbf{x}) = \sum_{\lambda} f(\lambda) K_{\lambda}(\mathbf{x}'|\mathbf{x})$, the present construction differs in how the reweighting factor is evaluated. In our scheme, the weight is evaluated conditionally on the realized value of λ , i.e., with respect to $r_{\lambda}(\mathbf{x}')$ rather than the marginal $r(\mathbf{x}')$. As a result, the computational cost remains governed by the sparsity of each individual kernel K_{λ} , rather than by the mixed kernel K_{mix} , which can be difficult to calculate or require an auxiliary Monte Carlo calculation. This randomized formulation therefore represents a trade-off: while it does not fully expand the support at the level of individual blur kernels, it preserves sparsity and remains computationally feasible in regimes where the deterministic construction becomes costly. As demonstrated in Sec. IV C, randomized blurred sampling successfully resolves cases in which Hamiltonian-induced blurred sampling fails to cure the QGT instability.

While the randomized formulation preserves sparsity and improves robustness in practice, its impact on the QGT estimator can be characterized more precisely. In particular, although the marginal distribution $r(\mathbf{x}')$ may explore the full Hilbert space, the reweighting factor is evaluated conditionally on the realized value of λ , namely with respect to $r_{\lambda}(\mathbf{x}')$. This conditioning leads to a modified structure of the QGT estimator, which we now make explicit. For convenience, we denote by supp_{λ} the support of the conditional distribution $r_{\lambda}(\mathbf{x}')$. We further introduce the indicator function

$$\mathcal{I}_{\lambda}(\mathbf{x}) = \begin{cases} 1, & \text{if } \mathbf{x} \in \text{supp}_{\lambda}, \\ 0, & \text{otherwise.} \end{cases} \quad (\text{A16})$$

In the infinite-sample limit, the QGT estimator obtained from randomized blurred sampling reads

$$\begin{aligned} S_{ij}^{\text{r-blur}} &= \left\langle \frac{\sum_{\mathbf{x}} \mathcal{I}_{\lambda}(\mathbf{x}) \langle \partial_{\theta_i} \psi_{\theta} | \mathbf{x} \rangle \langle \mathbf{x} | \partial_{\theta_j} \psi_{\theta} \rangle}{\langle \psi_{\theta} | \psi_{\theta} \rangle} \right\rangle_{\lambda} - \frac{\langle \partial_{\theta_i} \psi_{\theta} | \psi_{\theta} \rangle \langle \psi_{\theta} | \partial_{\theta_j} \psi_{\theta} \rangle}{\langle \psi_{\theta} | \psi_{\theta} \rangle \langle \psi_{\theta} | \psi_{\theta} \rangle} \\ &= \frac{\sum_{\mathbf{x}} \langle \mathcal{I}_{\lambda}(\mathbf{x}) \rangle_{\lambda} \langle \partial_{\theta_i} \psi_{\theta} | \mathbf{x} \rangle \langle \mathbf{x} | \partial_{\theta_j} \psi_{\theta} \rangle}{\langle \psi_{\theta} | \psi_{\theta} \rangle} - \frac{\langle \partial_{\theta_i} \psi_{\theta} | \psi_{\theta} \rangle \langle \psi_{\theta} | \partial_{\theta_j} \psi_{\theta} \rangle}{\langle \psi_{\theta} | \psi_{\theta} \rangle \langle \psi_{\theta} | \psi_{\theta} \rangle}. \end{aligned} \quad (\text{A17})$$

Compared with the exact QGT in Eq. (1), the deviation is

$$\Delta S_{ij} = \frac{\sum_{\mathbf{x}} \langle 1 - \mathcal{I}_{\lambda}(\mathbf{x}) \rangle_{\lambda} \langle \partial_{\theta_i} \psi_{\theta} | \mathbf{x} \rangle \langle \mathbf{x} | \partial_{\theta_j} \psi_{\theta} \rangle}{\langle \psi_{\theta} | \psi_{\theta} \rangle}. \quad (\text{A18})$$

Therefore, the estimator deviates from the exact QGT whenever $\langle \mathcal{I}_{\lambda}(\mathbf{x}) \rangle_{\lambda} \neq 1$.

Importantly, this deviation does not necessarily invalidate the resulting dynamics. We now show that, provided the variational ansatz is sufficiently expressive, randomized blurred sampling yields the exact projected TDVP evolution, despite modifying the QGT. The key observation is that the induced modification can be interpreted as a positive deformation of the Hilbert-space metric entering the TDVP principle.

Recall that the TDVP equation in Eq. (2) arises from minimizing the Hilbert-space distance between the variational tangent vector and the exact time-evolution direction. In the tangent space, these directions are given by

$$\begin{aligned} |\dot{\psi}_{\theta}\rangle_{\text{var}} &= \left(1 - \frac{|\psi_{\theta}\rangle \langle \psi_{\theta}|}{\langle \psi_{\theta} | \psi_{\theta} \rangle} \right) \frac{\sum_i |\partial_{\theta_i} \psi_{\theta}\rangle \dot{\theta}_i}{\langle \psi_{\theta} | \psi_{\theta} \rangle} \\ |\dot{\psi}_{\theta}\rangle_{\text{exact}} &= \left(1 - \frac{|\psi_{\theta}\rangle \langle \psi_{\theta}|}{\langle \psi_{\theta} | \psi_{\theta} \rangle} \right) \frac{-\xi \hat{H} |\psi_{\theta}\rangle}{\langle \psi_{\theta} | \psi_{\theta} \rangle}. \end{aligned} \quad (\text{A19})$$

The TDVP equation follows from minimizing the distance between these two tangent vectors,

$$\mathcal{L} = \| |\dot{\psi}_{\theta}\rangle_{\text{var}} - |\dot{\psi}_{\theta}\rangle_{\text{exact}} \|, \quad (\text{A20})$$

where the distance is defined through the Hilbert-space norm $\| \cdot \| \equiv \sum_{\mathbf{x}} | \cdot(\mathbf{x}) |^2$.

If we replace the standard Hilbert-space norm by the weighted norm $\| \cdot \|' \equiv \sum_{\mathbf{x}} \langle \mathcal{I}_{\lambda}(\mathbf{x}) \rangle_{\lambda} | \cdot(\mathbf{x}) |^2$, the resulting TDVP equation reproduces precisely the QGT obtained from randomized blurred sampling. This modification is therefore equivalent to a deformation of the underlying Hilbert-space metric. By construction, $\langle \mathcal{I}_{\lambda}(\mathbf{x}) \rangle_{\lambda} > 0$ for all \mathbf{x} , so the weighted norm remains strictly positive definite. Consequently,

$$\| |\dot{\psi}_{\theta}\rangle_{\text{var}} - |\dot{\psi}_{\theta}\rangle_{\text{exact}} \| = 0 \Leftrightarrow \| |\dot{\psi}_{\theta}\rangle_{\text{var}} - |\dot{\psi}_{\theta}\rangle_{\text{exact}} \|' = 0. \quad (\text{A21})$$

Therefore, if the variational ansatz is sufficiently expressive—namely, if there exists a parameter velocity $\dot{\boldsymbol{\theta}}^*$ such that $\| |\dot{\psi}_{\boldsymbol{\theta}} \rangle_{\text{var}} - |\dot{\psi}_{\boldsymbol{\theta}} \rangle_{\text{exact}} \| = 0$, then the same $\boldsymbol{\theta}^*$ also solves the TDVP equation defined with the modified norm, $\| |\dot{\psi}_{\boldsymbol{\theta}} \rangle_{\text{var}} - |\dot{\psi}_{\boldsymbol{\theta}} \rangle_{\text{exact}} \|' = 0$ and vice versa. Hence, randomized blurred sampling yields the correct parameter dynamics whenever the variational ansatz is sufficiently expressive.

In contrast, under support mismatch the standard VMC QGT corresponds to a deformation of the Hilbert-space metric with vanishing weights on configurations that are not sampled. The resulting metric therefore develops null directions and becomes degenerate, leading to potentially spurious dynamics even when the variational ansatz is sufficiently expressive. Randomized blurred sampling removes this degeneracy. Although the resulting QGT differs from the exact one, the induced metric remains strictly positive definite and spans the correct tangent directions. In this sense, randomized blurred sampling acts as a natural regularization of the QGT, restoring stability while preserving the correct projected dynamics.

Appendix B: Details of the parity mixing problem in TFIM

We study the dynamics of the initial state chosen as the equal-weight superposition of computational-basis states with even Z -parity,

$$|\psi_0\rangle = \sum_{\mathbf{x}} \frac{\hat{\mathcal{P}}_Z + 1}{2} |\mathbf{x}\rangle, \quad (\text{B1})$$

where $\hat{\mathcal{P}}_Z \equiv \prod_{i=1}^N Z_i$ denotes the Z -parity operator and $|\mathbf{x}\rangle$ are computational-basis states with $x_i \in \{\pm 1\}$. The time evolution is governed by the transverse-field Ising model (TFIM) Hamiltonian,

$$\hat{H}_{\text{TFIM}} = J \sum_{i=1}^N Z_i Z_{i+1} + h \sum_{i=1}^N X_i, \quad (\text{B2})$$

where periodic boundary conditions are assumed. In this setup, we are interested in how the Z -parity evolves under the dynamics, characterized by

$$\mathcal{P}_Z(t) = \frac{\langle \psi_0 | e^{i\hat{H}_{\text{TFIM}}t} \hat{\mathcal{P}}_Z e^{-i\hat{H}_{\text{TFIM}}t} | \psi_0 \rangle}{\langle \psi_0 | \psi_0 \rangle}. \quad (\text{B3})$$

In the following, we describe the variational ansätze employed—including the RBM and Gaussian ansatz—and present the analytic solution.

1. RBM ansatz and its initialization

We employ a restricted Boltzmann machine (RBM) with complex-valued parameters as the variational ansatz. The wavefunction is given by

$$\psi_{\text{RBM}}(\mathbf{x}) = \exp\left(\sum_{i=1}^N a_i x_i\right) \prod_{j=1}^M 2 \cosh\left(b_j + \sum_{i=1}^N W_{ij} x_i\right). \quad (\text{B4})$$

where a_i , b_j , and W_{ij} are complex parameters, and M denotes the number of hidden units. We define the ansatz size as $\alpha \equiv M/N$. The initialization is particularly simple. The action of the parity projector on a computational-basis state can be written as

$$\frac{\hat{\mathcal{P}}_Z + 1}{2} |\mathbf{x}\rangle = \cos\left(\frac{\pi}{4}\left(N - \sum_{i=1}^N x_i\right)\right) |\mathbf{x}\rangle. \quad (\text{B5})$$

Choosing the RBM parameters as $a_i = 0$, $b_1 = b_2 = i\pi N/4$, $W_{i1} = W_{i2} = -i(\pi/4)$ (with all other parameters set to zero), the RBM wavefunction exactly reproduces these amplitudes, thereby initializing the variational state to the chosen parity sector. For numerical stability, we add a small perturbation of order 10^{-3} to the parameters, ensuring that the logarithmic derivatives remain well defined.

2. Exact solution via mapping to Majorana fermions

It is well known that the one-dimensional TFIM can be mapped to a system of free fermions. Here we follow the mapping of Ref. [91] and directly introduce $2N$ Majorana fermions $\gamma_{2i}, \gamma_{2i+1}$. The spin operators are represented as

$$Z_{i+1} = (-i)^i \gamma_0 \gamma_1 \gamma_2 \cdots \gamma_{2i}, \quad X_{i+1} = -i \gamma_{2i} \gamma_{2i+1}. \quad (\text{B6})$$

One then obtains

$$Z_i Z_{i+1} = \begin{cases} -i \gamma_{2i-1} \gamma_{2i}, & \text{for } i < N, \\ i \hat{\mathcal{P}}_X \gamma_{2N-1} \gamma_0, & \text{for } i = N. \end{cases} \quad (\text{B7})$$

where $\hat{\mathcal{P}}_X = \prod X_i$ is the conserved X -parity operator. For even system size N , the initial state $|\psi_0\rangle$ lies in the sector $\hat{\mathcal{P}}_X = 1$. Restricting to this sector, the Hamiltonian becomes

$$\hat{H}_{\text{TFIM}} = -iJ \sum_{i=0}^{N-2} \gamma_{2i+1} \gamma_{2i+2} + iJ \gamma_{2N-1} \gamma_0 - ih \sum_i \gamma_{2i} \gamma_{2i+1}. \quad (\text{B8})$$

In this representation, the Z -parity operator reads

$$\mathcal{P} = (-i)^{N/2} \prod_{i=0}^{N/2-1} \gamma_{4i+1} \gamma_{4i+2}. \quad (\text{B9})$$

Although the Hamiltonian is quadratic in Majorana operators, so that the time-evolution operator is a fermionic Gaussian operator (a matchgate circuit), the initial state $|\psi_0\rangle$ is not Gaussian. We therefore exploit the symmetry of the Z -parity operator. Using the anticommutation relation $\{X_i, \hat{\mathcal{P}}_Z\} = 0$, which implies

$$\hat{\mathcal{P}}_Z \hat{H}_{\text{TFIM}}(J, h) = \hat{H}_{\text{TFIM}}(J, -h) \hat{\mathcal{P}}_Z, \quad (\text{B10})$$

we obtain

$$\begin{aligned} |\psi(t)\rangle &\equiv e^{-i\hat{H}_{\text{TFIM}}(J, h)t} |\psi_0\rangle \\ &= e^{-i\hat{H}_{\text{TFIM}}(J, h)t} \frac{\hat{\mathcal{P}}_Z + 1}{\sqrt{2}} |+\rangle \\ &= \frac{1}{\sqrt{2}} e^{-i\hat{H}_{\text{TFIM}}(J, h)t} |+\rangle + \frac{\hat{\mathcal{P}}_Z}{\sqrt{2}} e^{-i\hat{H}_{\text{TFIM}}(J, -h)t} |+\rangle. \end{aligned} \quad (\text{B11})$$

Since the state $|+\rangle$ is Gaussian—being the ground state of the quadratic Hamiltonian $-\sum_i X_i = \sum_i i \gamma_{2i} \gamma_{2i+1}$. Its time evolution under the quadratic TFIM Hamiltonian remains Gaussian. We denote $e^{-i\hat{H}_{\text{TFIM}}(J, h)t} |+\rangle$ as $|\psi_G^+(J, h, t)\rangle$. The full wavefunction can then be written as

$$|\psi(t)\rangle = \frac{1}{\sqrt{2}} |\psi_G^+(J, h, t)\rangle + \frac{\hat{\mathcal{P}}_Z}{\sqrt{2}} |\psi_G^+(J, -h, t)\rangle. \quad (\text{B12})$$

The time-dependent Z -parity becomes:

$$\begin{aligned} \mathcal{P}_Z(t) &= \text{Re} \langle \psi_G^+(J, -h, t) | \psi_G^+(J, h, t) \rangle \\ &\quad + \frac{1}{2} \langle \psi_G^+(J, h, t) | \hat{\mathcal{P}}_Z | \psi_G^+(J, h, t) \rangle \\ &\quad + \frac{1}{2} \langle \psi_G^+(J, -h, t) | \hat{\mathcal{P}}_Z | \psi_G^+(J, -h, t) \rangle. \end{aligned} \quad (\text{B13})$$

The problem thus reduces to evaluating (i) the overlap between two Gaussian states and (ii) the expectation value of $\hat{\mathcal{P}}_Z$ in a Gaussian state. The overlap of two general fermionic Gaussian states (without $U(1)$ symmetry) can be computed using Pfaffian techniques; we refer the interested reader to Ref. [90] for details. The operator $\hat{\mathcal{P}}_Z$ is a product of Majorana operators [cf. Eq. (B9)], and its expectation value in a Gaussian state can be expressed as a Pfaffian of the corresponding covariance matrix $G_{i,j} \equiv \langle \gamma_i \gamma_j \rangle$ as

$$\langle \prod_i \gamma_{\alpha_i} \rangle = \text{pf} [G_{\alpha_i, \alpha_j}]. \quad (\text{B14})$$

Therefore, the time evolution of the Z -parity can be computed analytically for system sizes far beyond the reach of exact diagonalization.

3. Gaussian ansatz and its initialization

As shown in the main text, the RBM ansatz combined with blurred sampling performs well up to system sizes $N \sim 8$, where we employ a relatively large network with $\alpha = 4$. For larger systems, however, the expressiveness of the ansatz becomes the primary bottleneck of the t-VMC approach. To disentangle this limitation from other algorithmic aspects of t-VMC, we consider an alternative Gaussian ansatz. This ansatz permits efficient evaluation of wavefunction amplitudes and is capable of representing the exact time-evolved state $|\psi(t)\rangle$ at all times:

$$|\psi_{\text{Gaussian}}\rangle = |G^1\rangle + \hat{\mathcal{P}}_Z |G^2\rangle, \quad (\text{B15})$$

where $|G^1\rangle$ and $|G^2\rangle$ are Gaussian states parameterized as

$$|G^{1,2}\rangle = e^{\theta_{ij}^{1,2} \gamma_i \gamma_j} |+\rangle, \quad (\text{B16})$$

with parameters $\theta^{1,2}$ being $2N \times 2N$ antisymmetric real matrices, each containing $N(2N-1)$ independent parameters.

The remaining task is to evaluate the amplitudes in the computational basis,

$$\langle \mathbf{x} | \psi_{\text{Gaussian}} \rangle = \langle \mathbf{x} | G^1 \rangle + \hat{\mathcal{P}}_Z \langle \mathbf{x} | G^2 \rangle. \quad (\text{B17})$$

However, the basis state $|\mathbf{x}\rangle$ is not Gaussian. Importantly, the wavefunction should preserve the X -parity, so that $\langle \mathbf{x} | \psi_{\text{Gaussian}} \rangle$ should be the same as $\langle \hat{\mathcal{P}}_X \mathbf{x} | \psi_{\text{Gaussian}} \rangle$. Consequently, we may work in the symmetric combination

$$|\mathbf{x}\rangle_+ \equiv \frac{1}{\sqrt{2}} |\mathbf{x}\rangle + \frac{1}{\sqrt{2}} |\hat{\mathcal{P}}_X \mathbf{x}\rangle \quad (\text{B18})$$

which is a Gaussian state. In fact, $|\mathbf{x}\rangle_+$ is the ground state of the quadratic Majorana Hamiltonian

$$i \sum_{i=0}^{N-2} x_{i+1} x_{i+2} \gamma_{2i+1} \gamma_{2i+2} - i x_N x_1 \gamma_{2N-1} \gamma_0. \quad (\text{B19})$$

This observation allows us to reformulate the amplitude evaluation entirely in terms of overlaps between Gaussian states, thereby enabling an efficient implementation within the t-VMC framework. For numerical stability at initialization, we add a small perturbation of order 10^{-3} to the parameter $\theta_{ij}^{1,2} = 0$ to ensure that the logarithmic derivatives remain well defined.

Appendix C: Details of the spin relaxation problem in the TFIM

We study the real-time dynamics of the total Z magnetization $\hat{\mathcal{Z}} = \sum_{i=0}^{N-1} Z_i$, starting from a computational-basis product state $|\mathbf{x}_0\rangle$ under the TFIM Hamiltonian. The time-dependent expectation value is

$$\mathcal{Z}(t) = \langle \mathbf{x}_0 | e^{i\hat{H}_{\text{TFIM}}(J,h)t} \hat{\mathcal{Z}} e^{-i\hat{H}_{\text{TFIM}}(J,h)t} | \mathbf{x}_0 \rangle. \quad (\text{C1})$$

1. Exact solution via mapping to Majorana fermions

Using the anticommutation relation $\{X_i, Z_i\} = 0$, one obtains $Z_i e^{-i\hat{H}_{\text{TFIM}}(J,h)t} = e^{-i(\hat{H}_{\text{TFIM}}(J,h) - 2hX_i)t} Z_i$, which allows us to rewrite

$$\mathcal{Z}(t) = \sum_i \langle \mathbf{x}_0 | e^{i\hat{H}(J,h)t} e^{-i(\hat{H}(J,h) - 2hX_i)t} Z_i | \mathbf{x}_0 \rangle. \quad (\text{C2})$$

Since $|\mathbf{x}_0\rangle$ is an eigenstate of every Z_i with eigenvalue $\mathbf{x}_0(i) \in \{\pm 1\}$, we obtain

$$\mathcal{Z}(t) = \sum_i \mathbf{x}_0(i) \langle \mathbf{x}_0 | e^{i\hat{H}(J,h)t} e^{-i(\hat{H}(J,h) - 2hX_i)t} | \mathbf{x}_0 \rangle. \quad (\text{C3})$$

To proceed, we decompose the initial state into definite X -parity sectors, $|\mathbf{x}_0\rangle = \frac{1}{\sqrt{2}}(|\mathbf{x}_0^+\rangle + |\mathbf{x}_0^-\rangle)$, which yields

$$\begin{aligned} \mathcal{Z}(t) = \frac{1}{2} \sum_i \mathbf{x}_0(i) & \left(\langle \mathbf{x}_0^+ | e^{i\hat{H}(J,h)t} e^{-i(\hat{H}(J,h)-2hX_i)t} | \mathbf{x}_0^+ \rangle \right. \\ & \left. + \langle \mathbf{x}_0^- | e^{i\hat{H}(J,h)t} e^{-i(\hat{H}(J,h)-2hX_i)t} | \mathbf{x}_0^- \rangle \right). \end{aligned} \quad (\text{C4})$$

In this form, each contribution has a well-defined X -parity and can therefore be evaluated efficiently using the Majorana fermionic representation of the TFIM.

2. Dressed RBM ansatz and its initialization

In the simulations, we employ a complex RBM with translation symmetry, denoted by $\psi_{\text{symm-RBM}}(\mathbf{x})$ (see the definition in NetKet [88]). For this symmetric RBM, we fix the visible bias parameter to zero and use a hidden-unit density $\alpha = 1$. When the RBM parameters are initialized close to zero ($\sim 10^{-3}$), the resulting wavefunction $\psi_{\text{symm-RBM}}(\mathbf{x})$ approximates a uniform superposition over configurations. However, this ansatz alone cannot represent the desired initial state, which has support only on the fully polarized all-down configuration.

To incorporate this structure, we augment the symmetric RBM with a sector-dependent factor $f_\phi(\mathbf{x})$, parameterized by $n+1$ complex parameters $\phi \in \mathbb{C}^{n+1}$:

$$\psi_\theta(\mathbf{x}) = f_\phi(\mathbf{x}) \psi_{\text{symm-RBM}}(\mathbf{x}), \quad f_\phi(\mathbf{x}) = \phi_{s(\mathbf{x})}. \quad (\text{C5})$$

Here $s(\mathbf{x}) \equiv (\sum_i x_i + n)/2$ denotes the spin sector of configuration \mathbf{x} . This construction assigns an independent complex amplitude to each spin sector, allowing the ansatz to selectively enhance or suppress entire sectors. In particular, setting $\phi_0 = 1$ and $\phi_s = 0$ for $s \neq 0$ yields a wavefunction supported entirely on the fully polarized all-down configuration $\mathbf{x} = (-1, -1, \dots, -1)$, corresponding to the $s = 0$ sector. In practice, to avoid exact zeros that may lead to numerical instabilities, we initialize $\phi_s = \epsilon = 10^{-5} \times 2^{-n/2}$ for $s \neq 0$, while fixing $\phi_0 = 1$ throughout the simulation. Since $f_\phi(\mathbf{x})$ is independent across spin sectors in this parameterization, we refer to it as the *uncorrelated* parameterization.

To further expose the bias of the quantum geometric tensor, we introduce correlations between different spin sectors in the parameterization. In particular, we couple the single-spin-up sector to another sector, thereby breaking the independence of sector amplitudes. Concretely, we define

$$f_\phi(\mathbf{x}) = \begin{cases} \phi_1 + \phi_3 & \text{if } s(\mathbf{x}) = 3 \\ \phi_{s(\mathbf{x})} & \text{otherwise,} \end{cases}$$

so that the amplitude of the $s = 3$ sector explicitly depends on ϕ_1 , introducing correlations between the $s = 1$ and $s = 3$ sectors. We refer to this as a *correlated* parameterization.

Under the TFIM Hamiltonian, the resulting state has the following support structure:

$$\begin{aligned} \text{supp}(\psi_\theta) & \approx \{\mathbf{x} \in \{\pm 1\}^n : s(\mathbf{x}) = 0\} \\ \text{supp}(\hat{H}_{\text{TFIM}}\psi_\theta) & \approx \{\mathbf{x} \in \{\pm 1\}^n : s(\mathbf{x}) \in \{0, 1\}\} \\ \text{supp}(\partial_{\phi_i} \psi_\theta(\mathbf{x}) \partial_{\phi_j} \psi_\theta(\mathbf{x})) & = \{\mathbf{x} \in \{\pm 1\}^n\}. \end{aligned}$$

This reveals a pronounced support-mismatch problem both in variational force and QGT estimators. In the following, we give further results to discuss the effectiveness of the blurred sampling method under both parameterizations.

3. QGT bias and support of the forces

In this section, we argue why the Hamiltonian-induced blur sampling of Fig. 6(a) still produces the correct dynamics despite the QGT support mismatch problem, and why it fails in Fig. 6(b). In Fig. 7 we calculate the eigenvalue spectrum of the QGT and investigate the support of the force vector in the corresponding eigenbasis. We see in panel (a) that without correlation in the ansatz (first row), the Hamiltonian-induced blur ($q_2 = 0$, second column) produces a QGT with extremely limited support, compared to the randomized blur ($q_2 = 0.2$, first column). This should result in a divergence in the dynamics from the correct result, but we see in Fig. 6(a) that this is not the case. The reason for this can be found in panel (b). We see that both blurred sampling schemes produce unbiased force vectors that are strongly peaked on a single mode for $t = 0$ and $t = 0.01$, with the support on other modes having $|\rho_k| < 10^{-8}$. Due to this lack support, the bias in the QGT does not affect the final force vector. However, when we look at the same quantities for the correlated ansatz (second row), a different picture emerges. For $t = 0.01$, we see that the force vector has significant support on a large number of eigenmodes, which now get amplified incorrectly due to the QGT bias. The consequences are immediate: the dynamics in Fig. 6(b) diverges around this point.

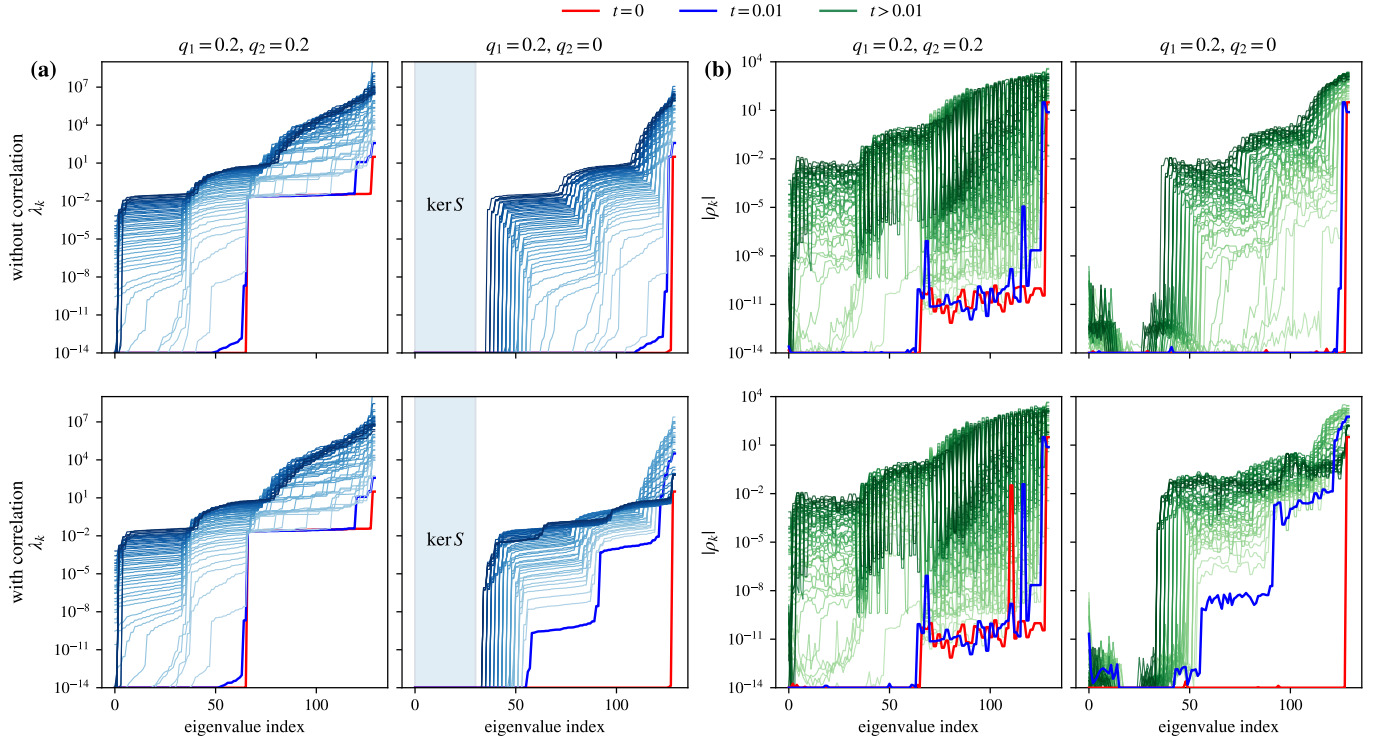


FIG. 7. Comparison of the support of the QGT and the force vectors for the t-VMC dynamics of Fig. 6 under blurred sampling. The first row corresponds to data for variational ansatz without correlation, whereas the second row corresponds to a variational ansatz with correlation between the spin sectors. (a) We diagonalize the QGT $\mathbf{S} = \mathbf{V}\mathbf{\Lambda}\mathbf{V}^\dagger$ and show the sorted eigenvalues λ_k over the duration of the dynamics, with lighter colors indicating earlier times $t \leq 0.5$. We highlight the times $t = 0$ and $t = 0.01$ with red and blue lines, respectively. Note that for the Hamiltonian-induced blur ($q_2 = 0$, second column), the QGT has a large kernel for the total duration of the dynamics. (b) We transform the force vector to the eigenbasis of the QGT: $\rho = \mathbf{V}^\dagger \mathbf{F}$ and show the components ρ_k for the four cases studied here. The components are not sorted in magnitude, but correspond directly to the ordering of the eigenvalues in (a).

Appendix D: Numerical details of t-VMC simulations

The most important part of t-VMC involves the regularization of the \mathcal{S} -matrix in Eq. 2 so that it can be stably inverted. For this, we use the regularizer by Schmitt [9] with the hyperparameters $\text{SNR}_{\text{cutoff}} = 2$, $\text{rcond} = 10^{-14}$ and $\text{rcond_smooth} = 10^{-10}$ for every experiment reported in this work. For sampling, we use Metropolis-Hastings MCMC with local updates depending on the Hamiltonian. In Table II we report the hyperparameters of the simulations. We emphasize that these are always kept exactly the same for the experiments with standard sampling and blurred sampling, hence any reported numerics differ only by the sampling scheme used. The code to reproduce all figures in this work can be found at [92]. Finally, we note that the simulations reported in Figures 2,3,4,5(a,b) and 6(a,b) were performed on a single NVIDIA RTX 6000 taking at most an hour of wall time. For Figure 5(c) we used 4 NVIDIA H100s, with simulations lasting several hours at most.

| Figure | Ansatz $ \psi_{\theta}\rangle$ | MCMC | Integrator | Miscellaneous |
|------------------------|---|--|--|--|
| Fig. 4(a) | $\alpha 0\rangle + \beta 1\rangle$ | 50% single flip 50% double flip $N_s = 8192$ | adaptive RK45 $\text{rtol} = 10^{-4}$ $\text{min } \delta t = 10^{-5}$ $\text{max } \delta t = 10^{-2}$ | |
| Fig. 4(b) | RBM $\alpha = 1/4$ See (B4) | Two-site exchange $N_s = 16384$ | Heun $\delta t = 10^{-3}$ | |
| Fig. 5(a,b) | RBM $\alpha = 4$ See (B4) | 50% single flip 50% double flip $N_s = 4096$ | adaptive RK45 $\text{rtol} = 10^{-4}$ $\text{min } \delta t = 10^{-5}$ $\text{max } \delta t = 10^{-2}$ | |
| Fig. 5(c) $h = 1/8$ | Gaussian Ansatz See (B17) | 50% single flip 50% double flip $N_s = 8192$ | Heun $\delta t = 4 \times 10^{-3}$ | Used JAXMg [93] for distributed eigensolve. Sampled $ \psi_{\theta} ^2$ in 32-bit precision [94]. |
| Fig. 5(c) $h = 1$ | Gaussian Ansatz See (B17) | 50% single flip 50% double flip $N_s = 8192$ | Heun $\delta t = 10^{-3}$ | Used JAXMg [93] for distributed eigensolve. Sampled $ \psi_{\theta} ^2$ in 32-bit precision [94]. |
| Fig. 6(a,b) | Dressed RBM $\alpha = 1$ See (C5) | 50% single flip 50% double flip $N_s = 4096$ | Heun $\delta t = 10^{-3}$ | |

TABLE II. Hyperparameters of t-VMC simulations